Magma mush chemistry at subduction zones, revealed by new melt major element inversion from calcic amphiboles

JING ZHANG[1,2], MADELEINE C.S. HUMPHREYS[1,*], GEORGE F. COOPER[1], JON P. DAVIDSON[1], AND COLIN G. MACPHERSON[1]

[1]Department of Earth Sciences, Durham University, Durham, DH1 3LE, UK

[2]State Key Laboratory of Lithospheric Evolution, Institute of Geology and Geophysics, Chinese Academy of Sciences, Beijing, 100029, China

* E-mail: madeleine.humphreys@durham.ac.uk

In memory of our friend and colleague, Jon Davidson

ABSTRACT

We have used multiple-regression methods to calibrate new, pressure-independent empirical chemometric equations to calculate the major element composition of basanitic to rhyolitic melts in equilibrium with calcic amphibole. The equations are based on amphibole stoichiometric formula components ± temperature from published experimental P-T-X data, and avoid some problems of previous studies associated with uncertainties in pressure determination. Compared with the pressure-dependent equations of Ridolfi and Renzulli (2012), tests run using an independent dataset indicate that the new equations yield improved precision and accuracy, in particular for SiO_2, TiO_2, CaO and K_2O. The results are only marginally more precise when temperature is used as a dependent variable, demonstrating

24 that temperature has a relatively minor role in controlling amphibole crystal chemistry
25 compared with melt composition. This allows us to accept a small decrease in precision in
26 excluding temperature from the analysis, which is very convenient for application of the
27 equations to natural amphiboles where temperature is typically unknown.

28 Using the new chemometric equations, reconstructed melt compositions in
29 equilibrium with the rims of amphiboles in pumice clasts of the Ongatiti ignimbrite are in
30 good agreement with coexisting matrix glass compositions, lending support for our analysis.
31 The compositionally variable cores of the amphiboles give predicted melt compositions with
32 large compositional variations from andesitic (63 wt% SiO_2) to high-Si rhyolite. These
33 compositional variations in the predicted melt compositions suggest that there may be a range
34 of heterogeneous melts undergoing progressive differentiation within a major crustal magma
35 storage region underneath the volcano. The results support the existence of genuine
36 intermediate composition melts within the storage region. Interaction between these stored
37 melts, disaggregating mush fragments and replenishing magmas gives rise to the chemical
38 complexity observed in erupted magmas. We also used our multiple regression model to
39 predict melts that were in equilibrium with amphiboles in plutonic nodules from Grenada
40 lavas. The predicted melts cover a wide range of compositions, perhaps as a result of in situ
41 fractionation, but are consistent with melt inclusions hosted in those cumulates, as reported
42 by Stamper et al. (2014). Overall, our new pressure- and temperature-independent equations
43 resolve issues associated with previous pressure-dependent studies and represent a useful tool
44 for further investigation of crustal processes at subduction zones.

45 **Keywords**: Calcic amphibole, chemometrics, melt compositions, multiple regression,
46 Ongatiti ignimbrite, plutonic xenoliths, Grenada.

47 # INTRODUCTION

48 Amphibole is a common, but chemically complex mineral phase present in many
49 hydrous arc magmas. Experimental studies show that amphibole crystallises over a large
50 range of pressure and temperature from diverse melts of basanitic to rhyolitic composition
51 (see below; Fig. 1a-d). The crystal chemistry of amphibole is sensitive to various magma
52 intensive variables (e.g. pressure, temperature, oxygen fugacity fO_2), as well as melt
53 composition and volatile content (e.g. Ridolfi and Renzulli 2012; Ridolfi et al. 2008, 2010).
54 Because of its broad stability range, amphibole has long been used for thermobarometry (e.g.
55 Anderson and Smith 1995; Blundy and Cashman 2008; Blundy and Holland 1990; Ernst and
56 Liu 1998; Hammarstrom and Zen 1986; Holland and Blundy 1994; Hollister et al. 1987;
57 Krawczynski et al. 2012; Molina et al. 2015; Putirka 2008, 2016; Ridolfi and Renzulli 2012;
58 Ridolfi et al. 2010; Schmidt, 1992). To begin with, amphibole-related barometers were
59 mainly based on the presence of a low-variance equilibrium assemblage. For example, the
60 Al-in-hornblende barometer requires the assemblage quartz + K-feldspar + plagioclase +
61 hornblende + biotite + Fe-Ti oxides + titanite + melt + fluid (e.g. Anderson and Smith 1995;
62 Hammarstrom and Zen 1986; Hollister et al. 1987). More recently, empirical amphibole-only
63 thermobarometers have been produced (Ridolfi and Renzulli 2012; Ridolfi et al. 2010), but
64 application of these barometers is limited by large offsets (e.g. up to 1,100 MPa) between
65 predicted pressure and experimental pressure (e.g. Erdmann et al. 2014; Putirka 2016; Shane
66 and Smith, 2013). This suggests that amphibole crystal chemistry is more sensitive to
67 temperature and melt composition than to pressure (Putirka 2016).

68 The same empirical thermobarometric formulations have been used to describe the
69 links between amphibole crystal chemistry and anhydrous melt major element composition,
70 using chemometric equations (Ridolfi and Renzulli 2012; see Eqs 5-11 therein). These
71 (pressure-dependent) empirical relationships enable melt SiO_2, TiO_2, Al_2O_3, FeO, MgO, CaO

72 and K_2O contents to be calculated from knowledge of amphibole major element formula
73 proportions and pressure. However, for natural igneous amphiboles, pressure is rarely known
74 independently, and given the uncertainty in pressures estimated from amphibole-only
75 barometer models (e.g. Ridolfi and Renzulli 2012) this could cause large uncertainties in the
76 inferred melt compositions. Furthermore, although Erdmann et al. (2014) demonstrate that
77 Ridolfi and Renzulli (2012)'s model yields reasonable melt SiO_2 content estimates for calcic
78 amphiboles crystallized from experimental melts with 55-75 wt % SiO_2 content, for calcic
79 amphiboles crystallized from more mafic melts, melt SiO_2 is overestimated by up to 15 wt %
80 (see below). Similar issues also exist in calculating melt TiO_2, FeO, CaO and K_2O contents.
81 Finally, although magma temperature is somewhat easier to determine petrologically than
82 pressure, temperature is also typically an unknown so we would ideally want to reconstruct
83 melt composition in the absence of both temperature and pressure terms.

84 In this study we have compiled an expanded dataset of previously published
85 experimental studies that crystallised amphibole. Using multiple regression analysis, we then
86 re-examine the compositional relationships between amphibole and melt, and generate new
87 chemometric equations with improved accuracy for SiO_2, TiO_2, FeO, CaO and K_2O,
88 compared with Ridolfi and Renzulli (2012). The accuracy of our chemometric equations is
89 tested using a second, independent experimental dataset. Importantly, our formulations are
90 independent of pressure and we propose models both with and without temperature terms.
91 This brings significant advantages in application of the equations to natural systems. We
92 apply the new equations to infer melt compositions coexisting with amphiboles erupted in the
93 Ongatiti ignimbrite, Taupo Volcanic Zone, New Zealand, and with plutonic amphiboles
94 preserved in xenoliths erupted from Grenada, Lesser Antilles.

SELECTING P-T-X DATA FROM LITERATURE

Experimental data from the Library of Experimental Phase Relations (LEPR) database (Hirschmann et al. 2008) and other studies were considered. We first split the data into two groups (Fig. 1a, c): one group for calibration (n=130, Table 1); and one group for test (n= 74, Table 1). The split of the experimental data from different references is random, and the two groups cover the same range of experimental P-T run conditions, melt compositions and the crystal chemistry of the experimentally produced amphiboles (except that the test group lacks kaersutite), demonstrating good representativeness of the test group. The calibration group also overlaps those datasets used in the previous studies of Ridolfi and Renzulli (2012) and Erdmann et al. (2014) (Table 1), whereas none of the data from the test group were used in these studies. Therefore, the test group can also be used as a direct, independent test of Ridolfi and Renzulli (2012)'s results. We applied two criteria to filter the data (see below): 1) the amphibole compositions must be calcic according to International Mineralogical Association (IMA; Hawthorne et al., 2012); 2) there must be amphibole-melt equilibrium as tested using the Fe-Mg exchange coefficient.

First, all the selected amphibole compositional data from the literature were recalculated from wt% oxide to formula proportions (atoms per formula unit/apfu), following the amphibole stoichiometry calculation procedure recommended by IMA (Leake et al. 1997). Si, Al, Ti, Cr, Fe, Mn, Mg were allocated to the tetrahedral (T) and small octahedral (M1-3) sites and Fe^{3+} and Fe^{2+} proportions were determined separately by charge balance, taking the approach of "average Fe^{3+}" as described by Schumacher (1997). This is important because the details of the ferric-ferrous calculations can affect other formula components, including Na_{M4} and thus A-site totals. Ca, Na and K were allocated to the large octahedral (M4) and vacant/partially-filled (A) sites. Any amphiboles classified as non-calcic (Ca_{M4} < 1.5 apfu) were discarded. The remaining calcic amphiboles are classified as edenite-pargasite (Parg),

hastingsite-magnesiohastingsite (MgHst), kaersutite - ferrokaersutite (Kaer), tschermakite-ferrotschermakite (Tsch) and magnesiohornblende (MgHbl) following Leake et al. (1997) (Table 1; Fig. 2). Amphiboles that failed to meet the standard of stoichiometry calculation of calcic amphibole were also discarded at this point.

Second, following Putirka (2016), we employed the Fe-Mg exchange coefficient $K_D(\text{Fe-Mg})^{\text{Amph-melt}}$ (simply K_D) to test whether equilibrium was achieved between amphiboles and coexisting melts during the experiments. K_D, expressed as:

$$K_D = \frac{X_{FeOt}^{Amph}}{X_{MgO}^{Amph}} \Big/ \frac{X_{FeOt}^{Melt}}{X_{MgO}^{Melt}}$$

(FeOt is total Fe as FeO). K_D is independent of temperature, pressure and co-crystallizing mineral phases (Putirka, 2016). Following Putirka (2016), we consider K_D values in the range of 0.28±0.11 as an indication of equilibrium. Any experimentally produced amphibole and melt compositions that fell outside this range were removed from the dataset (Fig. 3); we note that the samples that failed to meet this test for equilibrium did not fall into any particular range of experimental P-T conditions or melt chemistry (Fig. 1).

CALCIC AMPHIBOLE CRYSTALLIZATION CONDITIONS

The resultant dataset of experimental calcic amphiboles shows wide compositional variability ($5.7 < Si_T < 7.0$; $0 < Ti_{M1\text{-}3} < 0.8$; $0 < [Na+K]_A < 1.0$) over the range of experimental conditions (Fig. 2). The experimental dataset generally represents amphibole crystallization conditions in an evolving magmatic environment, from hot, mafic melt (950-1,100 °C, c.a. 40-60 wt % SiO_2) to cooler, felsic melt (800-950 °C, c.a. 60-78 wt % SiO_2) (Fig. 1c-d). Exceptions to this trend are present as outliers, for example the crystallisation of MgHbl from rhyolitic melts at temperatures up to 1050 °C (Sisson 1994) (Fig. 1d). We did

not examine the effect of variations in melt H_2O concentration or oxygen fugacity in this study. At low pressure, the crystallization of calcic amphiboles occurs over a large temperature range (750-1,050 °C) while at high pressure conditions (2-2.5 GPa) this range narrows and calcic amphiboles are linked to the highest temperatures (1,050-1,100 °C; Fig. 1b). This limitation is not unique to our dataset and was recognised by Ridolfi and Renzulli (2012). To some extent this range of conditions may reflect the stability of calcic amphiboles and the liquid line of descent of evolving magmas (Ridolfi and Renzulli 2012; Ridolfi et al. 2010), but may also simply represent the conditions of interest for recent experimental studies.

The crystallisation conditions of individual amphibole species are shown in Fig. 1d (pressure and temperature) and Fig. 4 (melt chemistry). Parg and MgHst dominate in the hottest, most mafic melts, while MgHbl is found only in cooler, more silicic melts (typically > 70 wt% SiO_2). Kaer crystallizes from melts with similar SiO_2 and Al_2O_3 contents to those MgHst-bearing melts, but with higher TiO_2 and lower CaO and MgO contents (Fig. 4a-b, d-e). The compiled dataset also demonstrates that MgHst, MgHbl and Tsch can all crystallize at the same pressure (e.g. 200 MPa; Fig. 1b). The poor correlation between pressure and amphibole tetrahedral Si and Al content (Si_T and Al_T, respectively) demonstrates the weak control by pressure on amphibole crystal chemistry (Putirka 2016); in contrast, amphibole Si_T is strongly correlated with melt SiO_2 and TiO_2 contents (e.g., Fig. 1f), and intermediately correlated with temperature (Fig. 1e), suggesting that melt compositions and temperature are more important controlling factors to amphibole compositions than pressure. The stronger correlation of amphibole Si_T against melt SiO_2 content than against temperature also indicates that melt chemistry is probably more important than temperature in controlling amphibole crystal chemistry (Putirka 2016).

MULTIPLE REGRESSION ANALYSIS

In order to investigate the relationships between melt major element compositions and amphibole crystal chemistry and temperature, we carried out a multiple regression (MR) analysis using the statistical software package R (R Core team 2013). The MR analysis allows the values of dependent variables to be predicted based on multiple input parameters (independent variables). The SiO_2, TiO_2, Al_2O_3, FeO, MgO, CaO, K_2O contents in the melt, normalized to 100% anhydrous, are treated as dependent variables. We initially inspected the entire calibration dataset and noticed that melt TiO_2, FeO, MgO, CaO all showed curving relationships with amphibole formula components; therefore we decided to use the natural logarithms of the concentration (e.g. $\ln TiO_2$, melt) as dependent variables. Failure to do this may yield negative calibration results at low concentrations. Similarly, for melt SiO_2 we identified a curving relationship with Si_T (amph) and therefore used $\ln(Si_T)$ as an independent variable for regression against melt SiO_2. For independent variables, we tested both amphibole-only and amphibole+T approaches, in order to decipher the significance of temperature in controlling amphibole crystal chemistry. The MR analyses were performed independently of pressure. Rather than using total formula proportions unassigned to different crystallographic sites (Ridolfi and Renzulli 2012), as independent compositional variables we used the stoichiometric components, including tetrahedral site Si (Si_T), M1-3 site Al (Al_{VI}), Fe^{3+}, Mg, Ti and Fe^{2+}, and M4 site Ca (Ca_{M4}), and A site Na (Na_A). We also tested regressions using Fe_T instead of ferric and ferrous components because of the uncertainties associated with calculation of Fe^{3+} and Fe^{2+} (Schumacher 1997), although with only one exception this did not appear as a significant parameter. Tetrahedral site Al (Al_T), which has commonly been treated as one of the key parameters in previous amphibole thermobarometry studies, was avoided as an independent variable, in order to avoid the issue of multicollinearity. This is because amphibole SiO_2 or Si_T are strongly correlated with melt

189 SiO_2 content (e.g. Fig. 1f), and the stoichiometric calculation method uses Al_T to fill the
190 tetrahedral site after accommodation of all available Si ($Si_T + Al_T = 8$ apfu), with excess Al
191 assigned to the octahedral sites (M1-3). We also did not consider Na_{M4}, for a similar reason
192 (Ca + Na = 2 apfu in M4, with excess Na assigned to the A site). We did not consider M1-3
193 site Cr and Mn, and A-site K, due to their minor abundances in amphibole and thus high
194 relative analytical uncertainties.

195 The output of each MR analysis is given as the intercept and coefficients of the
196 nominated independent variables, on which basis a multiple regression function can be
197 derived (Table 2). For example, *Eq. 1* used for calculating the SiO_2 content in the melt is
198 written as:

$$SiO_2\ (wt\ \%) = -228.000 - 0.0107T + 165.000\ \ln Si - 7.2190Mg \quad (Eq.\ 1)$$

199 Evaluation of each function was done based on the coefficient of determination (R^2),
200 standard error of the estimate (*SE*), number of objects/observations (*N*), and confidence of the
201 coefficients for each independent variable and constant (*p-value*). A correlation that we deem
202 to be statistically significant is reflected by $N \geq 30$, $R^2 \geq 0.6$ and *p-value* of each determined
203 coefficient < 0.01. In preference, we chose equations with fewer variables as this reduces the
204 propagated analytical uncertainty in applying the regressions to natural data. In Table 2, we
205 use the normal font to denote that the *p-values* of the MR-derived independent variables and
206 the constants are < 0.01 (>99% confidence), the bold font to denote that the *p-values* of the
207 corresponding independent variable/constant are in the range 0.01-0.03 (97-99% confidence).
208 The MR analysis was performed following a trial-and-error procedure: all independent
209 variables mentioned above were initially included in the MR analyses, then those with
210 highest *p-value* > 0.01 were progressively removed until all the remaining independent
211 variables and constants are statistically significant (mostly *p-value* <<0.01 in our calibrations).

We use the standard error of estimate (*SE*) to denote the precision of chemometric equations derived from MR analyses (Table 2). This is done by comparison of the predicted and measured data from the calibration dataset. To test the accuracy of the results, we applied the MR-derived equations to amphiboles from the test dataset to predict the compositions of their coexisting melts. Equivalent statistical parameters calculated for comparison of the test group with experimental melt compositions are denoted using lower case (e.g. r^2, *se*; Table 2) and are compared with those of the MR analysis. We regard *se* values (in wt % oxide) of corresponding chemometric equations as representative of the accuracy of the MR analyses, although *se* is typically lower than SE because of the more restricted compositional spread of the test dataset.

RESULTS

The major element compositions of the experimental melts can, in general, be linked with amphibole formula components ± experimental run temperature with robust R^2 (typically > 0.70) and reasonable precision (*SE*) and accuracy (*se*) (Table 2). In many cases, no statistically robust T-dependent parameterisation could be found. Otherwise, as expected, the addition of temperature as an independent variable slightly improves the precision of the MR equations, as revealed by decreasing *SE* and *se*, compared to those without including temperature as an independent variable (e.g. decrease of *SE* from 0.68 to 0.60 in the prediction of $\ln TiO_2$, *Eq. 5-6,* Table 2).

Moreover, our MR analyses results demonstrate the variable significance of amphibole major element formula proportions as the independent variables. Agreement of melt compositions of our calibration and test groups with experimental melt compositions is improved compared to Ridolfi and Renzulli (2012)'s study, which uses the total formula proportions of the major elements unassigned to different crystallographic sites, e.g. Al_{total}

instead of Al_T and Al_{VI}, Fe_{total} instead of Fe^{2+} and Fe^{3+}, Na_{total} instead of Na_{M4} and Na_A (see greater details below).

Melt SiO_2 content can be predicted robustly with two main groups of independent variables: lnSi + Al_{VI} + Fe^{3+} + Fe^{2+} + Ti + Ca ± Na_A ± Mg (*Eq. 1-2*), and lnSi + Mg ± T (*Eq. 3-4*). The melt SiO_2 contents of the test data are reproduced very well with $R^2 \geq 0.78$ (Fig. 6a), but in particular, the new equations are able to reproduce experimental melts with low SiO_2 contents (<55 wt%, data from Adam and Green 2006, Adam and Green 1994, Adam et al. 1993, Dalpé and Baker 2000, and Fujinawa and Green 1997), which failed to be reproduced with Ridolfi and Renzulli (2012)'s equations (Fig. 6a). One temperature-dependent equation was produced for Si and this brings only marginal increased precision and accuracy (*Eq.* 3, Table 2).

The natural logarithm of melt TiO_2 content can also be predicted robustly with the following group of independent variables: Si + Al_{VI} + Fe^{3+} + Fe^{2+} + Ca + Na_A ± T (Mg-absent group; *Eq. 5-6*). In general, the calibration results and test results are in excellent agreement with experimental melt TiO_2 content ($R^2 > 0.8$, Fig. 6b). The standard error is significantly smaller for the test population of data points and this is probably because of the more limited compositional range of amphiboles in this dataset (see Table 1). As for SiO_2, our equations also manage to reproduce the TiO_2 content of both calibration and test data points from the experiments with low melt SiO_2 content, where Ridolfi and Renzulli (2012)'s equation generates a large offset (cluster of points at ~ 2 wt% TiO_2, Fig. 6b).

The natural logarithm of melt FeO content can be predicted with two different groups of independent variables: Si + Al_{VI} + Fe^{3+} + Fe^{2+} + Ti + Ca (Mg-absent group; *Eq. 7*) and Si + Mg + Ca (*Eq. 8*). The calibrations are less robust than those for SiO_2 and TiO_2 (R^2 ~ 0.70) and no robust temperature-dependent regression was identified. The overall accuracy of our

FeO calibrations is similar to that of Ridolfi and Renzulli (2012), but with similar improvements in accuracy for melts with high FeO content (Fig. 6c), as for SiO_2 and TiO_2 (above).

Pressure is a very significant independent variable in Ridolfi and Renzulli (2012)'s model for melt MgO content (Fig. 5). At pressures >1 GPa (as calculated by Ridolfi and Renzulli (2012)'s barometer model), the predicted melt MgO is exponentially controlled by pressure, leading to drastic overestimation of melt MgO (Fig. 5). Even when the calculated pressure is <1 GPa and in good agreement with the experimental pressure, their calibration still generates significant scatter to high predicted melt MgO content (Fig. 5, 6g-h). In contrast, the results of our MR analyses suggest that the natural logarithm of melt MgO content can be predicted robustly with the independent variables Si + Al_{VI} + Mg (*Eq.9*; Fig. 6d), although, as for FeO, no robust T-dependent regression was identified. This small number of independent variables is in contrast with the model of Ridolfi and Renzulli (2012), which uses all amphibole major elements and pressure as independent variables. Our P-absent MgO predictions are very similar to those of Ridolfi for melts with MgO < 2 wt% but appear to be in much greater agreement with both calibration and test data for melts with higher MgO contents (R^2 = 0.80) than those of RR2012 (Fig. 6d).

For pressures > 1 GPa, as calculated using Ridolfi and Renzulli (2012)'s barometer, their equation for predicting melt CaO content produces a significant proportion of negative melt CaO contents. Our calibrations significantly improve the accuracy of predicted melt CaO content, particularly for more primitive melts and those at higher pressures (e.g. R^2 = 0.71, *Eq. 11*; Fig. 6e). We derive two groups of calibrations using CaO content and lnCaO, respectively; both groups are related to Si + Mg ± Al_{VI} ± Na_A (*Eq,* 10, 11). The two groups of calibrations generate results that are in good agreement with each other except at high melt

CaO contents, where *Eq. 10* starts to significantly underestimate CaO relative to the measured values; on balance, despite some scatter *Eq, 11* performs better over a wider range of compositions (as reflected by lower SE and higher R^2, Table 2; Fig. 6e).

Ridolfi and Renzulli (2012)'s equation for predicting melt K_2O content fails to reproduce the test and calibration data points from the low-melt SiO_2 content experiments, as for other elements (above), leading to significant over-estimation of melt K_2O for these compositions (Fig. 6f). In comparison, our calibrations give significant improvements in precision and accuracy for K_2O content in the experimental melts (R^2 = 0.628; *SE* = 0.59 wt %; *se* = 0.78 wt%; *Eq. 12, Fig. 6f*, Table 2), using Si + Al_{VI} + Mg + Fe^{3+} + Fe^{2+} + Ti + Ca + Na_A We also retrieved a robust regression using the parameter set Si+ Fe_T + Ti + Ca (*Eqn 13* although this has significantly lower predictive power (R^2 = 0.43, table 2). However, our *Eq. 12* still tends to underestimate melt K_2O at higher melt K_2O contents (> 3.0 wt %), with a small subset of otherwise apparently typical data plotting at anomalously low predicted melt K_2O (Fig. 6f).

For prediction of melt Al_2O_3 content, our best calibration is achieved using Al_{VI} + Mg + Fe^{3+} + Ti + Na_A (*Eq. 14*; Table 2). However, our calibration performs similarly to that of Ridolfi and Renzulli (2012) (R^2 = 0.59, SE = 0.93 wt%, Fig. 6g).

We did not find any robust regressions with an acceptable R^2 for melt Na_2O content; this finding is consistent with Ridolfi and Renzulli (2012) and we therefore do not attempt to predict melt Na_2O. We speculate that this lack of robust correlation could be due to problems with accurate electron microprobe analysis of Na in glass (Ridolfi and Renzulli 2012), or may arise if variable crystallisation of plagioclase from the host melts controls melt Na_2O content.

The *se* values for the test data are generally larger than *SE* for the calibration dataset, except for estimation of lnTiO_2, lnFeO and lnMgO. This is partly due to the smaller number

of analyses in the test group (n = 74 compared with n = 130 for the calibration group) and likely also in part because the range of melt TiO_2, FeO and MgO of the test experiments is slightly smaller than the calibration experiment group (with a slightly different balance of amphibole species, Table 1). The calibrations of melt K_2O and Al_2O_3 contents are the least robust among all calibrated elements (R^2 = 0.59 and 0.63, respectively, with high relative *SE* and *se Eq. 12-14*). In general, the effect of excluding temperature as an independent variable appears to be minimal, with no loss in accuracy over temperature-dependent results. This is important because the absence of both temperature and pressure in our calibrations is a major advantage in applying our results to natural systems, in which they are typically unknown.

IMPLICATIONS

Here we present two case studies to demonstrate how our chemometric equations may be applied to both volcanic and plutonic amphiboles: amphiboles in pumice clasts from the Ongatiti ignimbrite of Mangakino volcano, and in plutonic nodules from Grenada lavas.

Applications to amphiboles from the Ongatiti ignimbrite

Background The Ongatiti ignimbrite was erupted from Mangakino volcano, Taupo volcanic zone, New Zealand, at around 1.2 Ma (Houghton et al. 1995). The following summary is taken from the recent study of Cooper and Wilson (2014). The ignimbrite represents a large (>500 km^3 dense rock equivalent) unzoned deposit of crystal-rich rhyodacite to rhyolite magma, containing 20-30% crystals of plagioclase, quartz, orthopyroxene, amphibole, Fe-Ti oxides, zircon and apatite. Amphibole crystals from pumice clasts of the Ongatiti ignimbrite show variations in mineral textures coupled with varying chemical compositions. The majority of the amphiboles (83%) have resorbed, patchy zoned cores (Type B crystals), in contrast to Type A crystals, which are unzoned or only weakly

zoned. Both Types have oscillatory zoned, relatively homogeneous rims with similar composition to the Type A cores (MgHbl, $1.20 < Al_T < 1.42$; Fig. 7b, c). Type B cores have heterogeneous major and trace element compositions ($1.16 < Al_T < 2.10$, dominantly MgHst and MgHbl compositions with rare Tsch-Parg). The amphiboles coexist with homogeneous rhyolitic matrix glass (SiO_2 = 77.75 -78.63 wt %; Table 3; Fig. 8). It is suggested that the resorbed Type B amphibole cores were sourced from chemically variable crystal mushes that were disaggregated and transported by a later melt replenishment event, and brought into a final shallow storage region, where additional amphibole crystallisation occurred to form the Type A amphiboles and oscillatory zoned overgrowths (Cooper and Wilson 2014). In the following analysis we first assess the degree to which our amphibole chemometric equations can reproduce the major element compositions of matrix glasses. We then apply our equations to infer the chemical compositions of the mush melts from which the Type B cores grew, prior to disaggregation and possible partial dissolution during transport to the melt-dominant body.

Testing for reproduction of equilibrium matrix glass compositions The crystal rims of all amphiboles from Ongatiti are chemically homogeneous and textural evidence indicates that they are also in equilibrium with the matrix glass (Cooper and Wilson 2014). We therefore focus on attempting to reconstruct the compositions of matrix glasses in equilibrium with the rims of amphiboles from selected pumice clasts (GC1, P2023, P2026, P2027 and P2184, see Table 3; Cooper and Wilson 2014) using the temperature-independent equations from Table 2. The resulting predicted melt compositions are given in Table 3 and plotted in Fig. 8. In general, the calculated melt compositions agree well with the measured matrix glass compositions, within the *SE* of the corresponding MR equations. Predicted Al_2O_3 compositions are in less good agreement, systematically ~1.5 wt% higher than those of the measured matrix glass compositions. This is probably related to the overestimation of

356 melt Al_2O_3 with *Eq. 19* at low melt Al_2O_3 content (see Fig. 6g). We note that the predicted
357 melt CaO, MgO and FeO concentrations are in very good agreement with the low-SiO_2 end
358 of the spread of measured glass compositions. This could be explained if the amphibole
359 equilibrated with the melt before minor microlite crystallisation took place. Overall, the
360 results demonstrate good reliability of our chemometric equations in predicting melt major
361 element compositions and supports the conclusion derived by Cooper and Wilson (2014)'s
362 study that the homogeneous rims of amphiboles are in equilibrium with the melts prior to the
363 eruption.

364 **Predicted melt compositions in equilibrium with amphibole cores** We now use our
365 MR-derived chemometric equations to predict the compositions of melts in equilibrium with
366 the cores of Type B amphiboles, which display complex patchy zoning texture and large
367 compositional variations and were inferred to have formed in a chemically heterogeneous
368 crystal mush (Cooper and Wilson 2014). The results are plotted in Fig. 8 and indicate that the
369 cores of Ongatiti Type B amphiboles are nominally in equilibrium with melts spanning a
370 large compositional range from ~63-80 wt % SiO_2, 0.1-0.7 wt% TiO_2, ~1-5 wt% FeO and ~2-
371 5 wt % K_2O (Fig. 8). The inferred melts form an array comprising two groups as a result of
372 the presence of both MgHbl (with >44 wt% SiO_2 and < 9 wt% Al_2O_3) and MgHst (with <44
373 wt% SiO_2 and typically > 10 wt% Al_2O_3) within the Type B cores. Our key assumption is
374 that each amphibole analysis remained in equilibrium with the melt from which it crystallised
375 and therefore represents a snapshot of past melts that may no longer exist. However, some of
376 the crystal cores show gradational variations in greyscale in BSE images (see Fig. 7b) that
377 could represent partial solid-state diffusive equilibration. Before making any petrogenetic
378 interpretations about the inferred snapshot melt compositions we must therefore exclude the
379 possibility that any significant Fe-Mg interdiffusion may be modifying the predicted melt
380 compositions.

Intra-grain Fe-Mg diffusion could affect the validity of calculated melt compositions because both Mg_{M1-3} and Fe_{M1-3} may be present in the chemometric equations, and have different coefficients (see Table 2). At this stage, we exclude significant diffusion in other elements because, although very few diffusivity data for amphibole are currently available, comparison with olivine, clinopyroxene and orthopyroxene suggests that Fe-Mg interdiffusion is orders of magnitude quicker than for other elements (Allan et al. 2013). In order to quantify the potential variation in calculated melt compositions that might arise in response to Fe-Mg interdiffusion, we take two amphibole core compositions as examples (Fig. 8). The initial compositions are a MgHst with 41.83 wt% SiO_2, 11.62 wt% Al_2O_3 and molar Mg# 0.67, and a MgHbl with 44.65 wt% SiO_2, 7.66 wt% Al_2O_3 and Mg# 0.57 (see Table 4). We then arbitrarily modify their Mg# within the observed range in the natural amphibole dataset (0.90 to 0.10) and recalculate the predicted melts. The results are shown as vectors in Fig. 8. The diffusion-related variations fall close to the arrays of predicted melts for TiO_2, CaO, K_2O and MgO (Fig. 8a, d, e, f), but cut across the arrays for melt FeO and Al_2O_3 (Fig. 8b, c). This suggests that Fe-Mg interdiffusion is not extensive amongst the Ongatiti amphiboles, otherwise the calculated melt compositions would show scattered variations in Fe and Al. Although some effect of minor Fe-Mg interdiffusion is possible within the uncertainties of the predicted melt compositions, it is clear that the full range of predicted melts far exceeds any apparent variability that could arise due to diffusion. We therefore take confidence in the calculated melt compositions inferred to have been in equilibrium with the amphibole cores.

Cooper and Wilson (2014) concluded that the large compositional diversity in Ongatiti amphiboles is related to compositional variations in heterogeneous crystal mushes over a range of pressure-temperature conditions. Our analysis supports this hypothesis, and suggests that the MgHst amphibole cores crystallised from less evolved melts with 63-70 wt%

406 SiO_2 and 2.5-5 wt% FeO. The patchy texture (Figure 5 of Cooper and Wilson 2014) probably
407 arises by partial dissolution during ascent with the replenishing magma (e.g. Humphreys et al.
408 2006a) and new MgHbl then starts to crystallise from the eventual melt which has an initial
409 composition of ~73 wt% SiO_2 and 2 wt% FeO. Further differentiation of the replenishing
410 magma during shallow storage gives rise to increasingly silicic melts with >73 wt% SiO_2 (Fig.
411 8).

412 Our analysis therefore suggests that the Mangakino crustal storage region hosted
413 progressively differentiated melts of andesitic (~63 wt% SiO_2) to rhyolitic composition.
414 Within uncertainty, there is an almost continuous spread of inferred compositions and no
415 significant compositional gap; however the compositions of the predicted melts are bimodal
416 in abundance (Fig. 8). Our inferred melts are consistent with the compositions of a global
417 dataset of arc melt inclusions, but represent melts that are rarely sampled in the melt inclusion
418 record (60-70 wt% SiO_2, Reubi & Blundy 2009). This interpretation is interesting because it
419 is in contrast with a wealth of previous studies that suggested that andesites are largely a
420 result of mixing between mafic and silicic magmas, combined with mechanical incorporation
421 of a crystal load (e.g. Eichelberger et al. 2006; Humphreys et al. 2006a; Reubi and Blundy
422 2009). However, the andesitic melts in the Mangakino volcanic plumbing system are
423 probably short-lived and are not sampled by eruption at the surface. Without further textural
424 information linked explicitly to measured amphibole compositions we cannot comment
425 further on the likely spatial or temporal distribution of the varying melt compositions within
426 the heterogeneous crystal mush beneath Mangakino volcano. However, this approach seems
427 worthy of further investigation as an alternative means to examine the nature of crustal
428 storage and melt differentiation in arcs.

Applications to amphiboles in plutonic xenoliths from Grenada

Our second case study for application of the new chemometric equations is that of the abundant plutonic xenoliths erupted in lavas from Grenada, Lesser Antilles, as described by Stamper et al. (2014) and summarised below. The xenoliths are dominated by mafic minerals, including amphibole, and their bulk compositions are consistent with a cumulate origin. The origin of the xenoliths has been studied experimentally and using MELTS modelling, and interpreted as the progressive crystallisation sequence ol + sp, + cpx, + hbl, + plag, forming under hydrous conditions at 200-500 MPa, and with relatively small variations in host melt chemistry and temperature. The existence of robust independent experimental and modelling results for these cumulate rocks (Stamper et al. 2014) gives us a valuable opportunity to evaluate the applicability of our chemometric equations to plutonic amphiboles. Amphiboles are abundant in the majority of the xenoliths and in the andesitic host lavas, and most of the major element analyses indicate MgHst compositions, with occasional presence of Tsch and Parg (Stamper et al. 2014). Texturally, amphiboles in the xenoliths are present either as poikilitic interstitial crystals with inclusions of olivine, clinopyroxene, spinel and plagioclase, or as euhedral and equant crystals. Both types of amphiboles can be found in the amphibole-bearing cumulate nodules and lavas. To quantify the melt compositions that were in equilibrium with the cumulate crystals, we used published amphibole analyses from the xenoliths studied by Stamper et al. (2014) and calculated their corresponding melt compositions. The samples include clinopyroxenites (GRN17, GRN24, GR17, GR29, GR5-1), hornblendites (GR15, GR25, GR11, GR52), hornblende gabbro (GRN6, GRN 21, GRN5), as well as one non-cumulate hornblende gabbro (GR42). The results are all included in the Appendix Table 1.

Although the ranges are overlapping, the results show a general trend of increasing calculated melt SiO_2 contents from the more evolved cumulates, with the non-cumulate

454 gabbro yielding the highest melt SiO_2 (Fig. 9a). Amphiboles in clinopyroxenite give
455 calculated melts with 52-60 wt% SiO_2 and 2.2-6.1 wt% MgO; amphiboles from the
456 hornblendites give calculated melts with 52.9-62.6 wt% SiO_2 and 1.5-7.0 wt% MgO;
457 amphiboles from the cumulate gabbros give calculated melts with 54.3-63.1 wt% SiO_2 and
458 1.8-4.3 wt% MgO; and the non-cumulate gabbro gives calculated melts with 58.1-70.8 wt%
459 SiO_2 and 0.6-2.9 wt% MgO (Fig. 9f). Each individual sample occupies a part of these overall
460 arrays. As with Ongatiti, the extent of any possible diffusive re-equilibration is probably
461 small because Fe-Mg interdiffusion modelling results, displayed as vectors in Fig. 8, are
462 inconsistent with variation trends of the predicted melt Al_2O_3 and FeO compositions. In
463 comparison with melts calculated using the formulations of Ridolfi and Renzulli (2012), our
464 compositions span a similar range of SiO_2 but with significantly higher and less scattered
465 CaO (Fig. 9g), and slightly lower FeO (Fig. 9e). Inferred MgO concentrations cannot be
466 compared easily due to the use of the pressure term for RR2012, which performs poorly (see
467 Stamper et al. 2014 and Fig. 9f). This emphasises the advantage of our study in using
468 pressure-independent (and temperature-independent) equations for melt chemistry. For TiO_2,
469 the majority of the melts calculated using RR2012 fall on a steeper gradient with respect to
470 SiO_2, compared with those calculated using our equations (Fig. 9c). Some of our calculated
471 melts are offset to higher TiO_2; this is a result of slight differences in TiO_2 concentration in
472 the raw amphibole analyses. A larger subset of the melts calculated using RR2012 have
473 similarly high TiO_2, but these are not obviously linked to any compositional signature except
474 those amphiboles with lower SiO_2 (Fig. 9c).

475 In general, the calculated melt compositions are also broadly in agreement with the
476 (strongly scattered) compositions of clinopyroxene-hosted melt inclusions measured by
477 Stamper et al. (2014) (Fig. 9). In particular, the melts inferred from amphibole in the non-
478 cumulate hornblende gabbro agree very well with the most evolved pyroxene-hosted melt

inclusion, from a (different) non-cumulate gabbro (Stamper et al. 2014; Fig. 9b-h). The predicted melt compositions are also similar to the compositions of C-series lavas, and consistent with low-pressure fractionation trend derived from MELTS modelling (Stamper *et al.*, 2014; see Fig. 22 therein; Fig. 9b). These observations all indicate that our chemometric equations are able to make reliable predictions of melt chemistry from amphibole major element compositions.

Our predicted MgO concentrations project back towards the parental melts required to form the clinopyroxenite - hornblendite - hornblende gabbro assemblages (Fig. 9f; i.e. 47.5-51.3 wt % SiO_2 and 4.4-9.7 wt % MgO based on previous experimental studies, Stamper et al. 2014). These source melts are more mafic than our predicted melt compositions and the majority of the measured melt inclusions hosted in cumulate mineral phases (Stamper *et al.*, 2014). We propose two possible reasons to explain this offset as follows. Firstly, the large spread in our predicted melt compositions, and the melt inclusions, may reflect in situ melt evolution during protracted crystallization of the cumulate mineral phases. This progressive in situ fractionation can result in continuous and progressive changes to the residual interstitial melt hosted in the cumulate, and therefore formation of new interstitial phases and strongly zoned mineral overgrowths. Chemometric inversions using those zoned minerals would predict an array of melt compositions for each sample, as observed in our dataset. Unfortunately, there is insufficient detail about the textural locations of each amphibole analysis from Stamper et al. (2014) to test this rigorously. Secondly, the appearance of mineral phases in the plutonic xenoliths follows the sequence olivine, clinopyroxene, amphibole and plagioclase with decreasing temperature (Stamper et al. 2014). In contrast, our chemometric equations can only predict melt compositions that coexisted with amphibole, so we invariably miss an early part of this liquid line of descent. We would therefore expect the most primitive melts, i.e., those present during formation of the wehrlite cumulates and those

from the earlier stages of formation of the clinopyroxenite and hornblendite cumulates, to be absent from our results. However, overall our results indicate the differentiation of mafic to intermediate magmas within the crust under Grenada.

ACKNOWLEDGEMENTS

This work forms part of the first author's PhD research, which was funded by a Durham Doctoral Studentship (Durham University) and China Scholarship Council (201206170178). Madeleine Humphreys was supported by a Royal Society University Research Fellowship. George Cooper was supported by a NERC Postdoctoral Fellowship. We thank Kate Saunders and Yaoling Niu for their comments on an earlier version of this manuscript, and Adam Kent for useful discussions. We also acknowledge helpful journal reviews from Saskia Erdmann, Mike Rowe and an anonymous reviewer, and editorial assistance from Georg Zellmer.

REFERENCES

Adam, J., and Green, T. (2006). Trace element partitioning between mica- and amphibole-bearing garnet lherzolite and hydrous basanitic melt: 1. Experimental results and the investigation of controls on partitioning behaviour. Contributions to Mineralogy and Petrology, 152, 1-17.

Adam, J., and Green, T.H. (1994). The Effects of Pressure and Temperature on the Partitioning of Ti, Sr and REE between Amphibole, Clinopyroxene and Basanitic Melts. Chemical Geology, 117, 219-233.

Adam, J., Green, T.H., and Sie, S.H. (1993). Proton Microprobe Determined Partitioning of Rb, Sr, Ba, Y, Zr, Nb and Ta between Experimentally Produced Amphiboles and Silicate Melts with Variable F Content. Chemical Geology, 109, 29-49.

527 Allan, A.S.R., Morgan, D.J., Wilson, C.J.N ., and Millet, M. (2013). From mush to eruption
528 in centuries: assembly of the super-sized Oruanui magma body. Contributions to
529 Mineralogy and Petrology, 166, 143-164.
530 Alonso-Perez, R., Muntener, O., and Ulmer, P. (2009). Igneous garnet and amphibole
531 fractionation in the roots of island arcs: experimental constraints on andesitic liquids.
532 Contributions to Mineralogy and Petrology, 157, 541-558.
533 Anderson, J.L., and Smith, D.R. (1995). The Effects of Temperature and f(O_2) on the Al-in-
534 Hornblende Barometer. American Mineralogist, 80, 549-559.
535 Arculus, R.J., and Wills, K.J.A. (1980). The Petrology of Plutonic Blocks and Inclusions
536 from the Lesser Antilles Island Arc. Journal of Petrology, 21, 743-799.
537 Barclay, J., and Carmichael, I.S.E. (2004). A hornblende basalt from western Mexico: Water-
538 saturated phase relations constrain a pressure-temperature window of eruptibility.
539 Journal of Petrology, 45, 485-506.
540 Blatter, D.L., and Carmichael, I.S.E. (2001). Hydrous phase equilibria of a Mexican high-
541 silica andesite: A candidate for a mantle origin? Geochimica et Cosmochimica Acta,
542 65, 4043-4065.
543 Blundy, J., and Cashman, K. (2008). Petrologic Reconstruction of Magmatic System
544 Variables and Processes. Reviews in Mineralogy and Geochemistry, 69, 179-239.
545 Blundy, J.D., and Holland, T.J.B. (1990). Calcic Amphibole Equilibria and a New
546 Amphibole-Plagioclase Geothermometer. Contributions to Mineralogy and Petrology,
547 104, 208-224.
548 Bogaerts, M., Scaillet, B., and Auwera, J. V. (2006). Phase equilibria of the lyngdal
549 granodiorite (Norway): Implications for the origin of metaluminous ferroan granitolds.
550 Journal of Petrology, 47, 2405-2431.

551 Carroll, M.R., and Wyllie, P.J. (1989). Experimental Phase-Relations in the System Tonalite-
552 Peridotite-H2o at 15 Kb - Implications for Assimilation and Differentiation Processes
553 near the Crust-Mantle Boundary. Journal of Petrology, 30, 1351-1382.
554 Cashman, K., and Blundy, J. (2013). Petrological cannibalism: the chemical and textural
555 consequences of incremental magma body growth. Contributions to Mineralogy and
556 Petrology, 166, 703-729.
557 Chakraborty, S. (1997). Rates and mechanisms of Fe-Mg interdiffusion in olivine at 980º-
558 1300ºC. Journal of Geophysical Research-Solid Earth, 102, 12317-12331.
559 Cooper, G.F., and Wilson, C.J.N. (2014). Development, mobilisation and eruption of a large
560 crystal-rich rhyolite: The Ongatiti ignimbrite, New Zealand. Lithos, 198, 38-57.
561 Costa, F., Scaillet, B., and Pichavant, M. (2004). Petrological and experimental constraints on
562 the pre-eruption conditions of Holocene dacite from Volcan San Pedro (36°S, Chilean
563 Andes) and the importance of sulphur in silicic subduction-related magmas. Journal of
564 Petrology, 45, 855-881.
565 Dalpé, C., and Baker, D.R. (2000). Experimental investigation of large-ion-lithophile-
566 element-, high-field-strength-element- and rare-earth-element-partitioning between
567 calcic amphibole and basaltic melt: the effects of pressure and oxygen fugacity.
568 Contributions to Mineralogy and Petrology, 140, 233-250.
569 Davidson, J., Turner, S., Handley, H., Macpherson, C., and Dosseto, A. (2007). Amphibole
570 "sponge" in arc crust? Geology, 35, 787-790.
571 Erdmann, S., Martel, C., Pichavant, M., and Kushnir, A. (2014). Amphibole as an archivist of
572 magmatic crystallization conditions: problems, potential, and implications for
573 inferring magma storage prior to the paroxysmal 2010 eruption of Mount Merapi,
574 Indonesia. Contributions to Mineralogy and Petrology, 167, 1-23.

575 Ernst, W.G., and Liu, J. (1998). Experimental phase-equilibrium study of Al- and Ti-contents
576 of calcic amphibole in MORB - A semiquantitative thermobarometer. American
577 Mineralogist, 83, 952-969.
578 Fujinawa, A., and Green, T.H. (1997). Experimental study of partitioning of Hf and Zr
579 between amphibole, clinopyroxene, garnet, and silicate melts. Journal of Mineralogy
580 Petrology and Economic Geology, 2, 69-89 (in Japanese).
581 Gardner, J.E., Rutherford, M., Carey, S., and Sigurdsson, H. (1995). Experimental
582 Constraints on Pre-Eruptive Water Contents and Changing Magma Storage Prior to
583 Explosive Eruptions of Mount St-Helens Volcano. Bulletin of Volcanology, 57, 1-17.
584 Green, T.H., and Pearson, N.J. (1985). Experimental-Determination of Ree Partition-
585 Coefficients between Amphibole and Basaltic to Andesitic Liquids at High-Pressure.
586 Geochimica et Cosmochimica Acta, 49, 1465-1468.
587 Grove, T.L., DonnellyNolan, J.M., and Housh, T. (1997). Magmatic processes that generated
588 the rhyolite of Glass Mountain, Medicine Lake volcano, N California. Contributions
589 to Mineralogy and Petrology, 127, 205-223.
590 Grove, T.L., Elkins-Tanton, L.T., Parman, S.W., Chatterjee, N., Muntener, O., and Gaetani,
591 G.A. (2003). Fractional crystallization and mantle-melting controls on calc-alkaline
592 differentiation trends. Contributions to Mineralogy and Petrology, 145, 515-533.
593 Hammarstrom, J.M., and Zen, E.A. (1986). Aluminum in Hornblende: an Empirical Igneous
594 Geobarometer. American Mineralogist, 71, 1297-1313.
595 Hawthorne, F.C., Oberti, R., Harlow, G.E., Maresch, W.V., Martin, R.F., Schumacher, J.C.,
596 and Welch, M.D. (2012). Nomenclature of the amphibole supergroup. American
597 Mineralogist, 97, 2031-2048.
598 Hilyard, M., Nielsen, R.L., Beard, J.S., Patino-Douce, A., and Blencoe, J. (2000).
599 Experimental determination of the partitioning behavior of rare earth and high field

600 strength elements between pargasitic amphibole and natural silicate melts.
601 Geochimica et Cosmochimica Acta, 64, 1103-1120.
602 Hirschmann, M.M., Ghiorso, M.S., Davis, F.A., Gordon, S.M., Mukherjee, S., Grove, T.L.,
603 Krawczynski, M., Medard, E., and Till, C.B. (2008). Library of Experimental Phase
604 Relations (LEPR): A database and Web portal for experimental magmatic phase
605 equilibria data. Geochemistry, Geophysics, Geosystems, 9, 1711-1730.
606 Holland, T., and Blundy, J. (1994). Nonideal Interactions in Calcic Amphiboles and Their
607 Bearing on Amphibole-Plagioclase Thermometry. Contributions to Mineralogy and
608 Petrology, 116, 433-447.
609 Hollister, L.S., Grissom, G.C., Peters, E.K., Stowell, H.H., and Sisson, V.B. (1987).
610 Confirmation of the Empirical Correlation of Al in Hornblende with Pressure of
611 Solidification of Calc-Alkaline Plutons. American Mineralogist, 72, 231-239.
612 Holtz, F., Sato, H., Lewis, J., Behrens, H., and Nakada, S. (2005). Experimental petrology of
613 the 1991-1995 Unzen dacite, Japan. Part I: Phase relations, phase composition and
614 pre-eruptive conditions. Journal of Petrology, 46, 319-337.
615 Houghton, B.F., Wilson, C.J.N., McWilliams, M.O., Lanphere, M.A., Weaver, S.D., Briggs,
616 R.M., and Pringle, M.S. (1995). Chronology and dynamics of a large silicic magmatic
617 system: central Taupo Volcanic Zone, New Zealand. Geology, 23, 13-16.
618 Huber, C., Bachmann, O., and Manga, M. (2009). Homogenization processes in silicic
619 magma chambers by stirring and mushification (latent heat buffering). Earth and
620 Planetary Science Letters, 283, 38-47.
621 Humphreys, M.C.S., Blundy, J.D., and Sparks, R.S.J. (2006a). Magma Evolution and Open-
622 System Processes at Shiveluch Volcano: Insights from Phenocryst Zoning. Journal of
623 Petrology, 47, 2303-2334.

624 Humphreys, M.C.S., Kearns, S.L., and Blundy, J.D. (2006b). SIMS investigation of electron-
625 beam damage to hydrous, rhyolitic glasses: Implications for melt inclusion analysis.
626 American Mineralogist, 91, 667-679.
627 Kawamoto, T. (1996). Experimental constraints on differentiation and H_2O abundance of
628 calc-alkaline magmas. Earth and Planetary Science Letters, 144, 577-589.
629 Klein, M., Stosch, H.G., and Seck, H.A. (1997). Partitioning of high field-strength and rare-
630 earth elements between amphibole and quartz-dioritic to tonalitic melts: An
631 experimental study. Chemical Geology, 138, 257-271.
632 Klugel, A. (2001). Prolonged reactions between harzburgite xenoliths and silica-
633 undersaturated melt: implications for dissolution and Fe-Mg interdiffusion rates of
634 orthopyroxene. Contributions to Mineralogy and Petrology, 141, 1-14.
635 Krawczynski, M.J., Grove, T.L., and Behrens, H. (2012). Amphibole stability in primitive arc
636 magmas: effects of temperature, H_2O content, and oxygen fugacity. Contributions to
637 Mineralogy and Petrology, 164, 317-339.
638 Leake, B.E., Woolley, A.R., Arps, C.E.S., Birch, W.D., Gilbert, M.C., Grice, J.D.,
639 Hawthorne, F.C., Kato, A., Kisch, H.J., Krivovichev, V.G., and others (1997).
640 Nomenclature of amphiboles: Report of the subcommittee on amphiboles of the
641 International Mineralogical Association, Commission on New Minerals and Mineral
642 Names. Canadian Mineralogist, 35, 219-246.
643 Martel, C., Champallier, R., Prouteau, G., Pichavant, M., Arbaret, L., Balcone-Boissard, H.,
644 Boudon, G., Boivin, P., Bourdier, J.L., and Scaillet, B. (2013). Trachyte Phase
645 Relations and Implication for Magma Storage Conditions in the Chaine des Puys
646 (French Massif Central). Journal of Petrology, 54, 1071-1107.
647 Molina, J.F., Moreno, J.A., Castro, A., Rodríguez, C., and Fershtater, G.B. (2015). Calcic
648 amphibole thermobarometry in metamorphic and igneous rocks: New calibrations

649 based on plagioclase/amphibole Al-Si partitioning and amphibole/liquid Mg
650 partitioning. Lithos, 232, 286-305.
651 Moore, G., and Carmichael, I.S.E. (1998). The hydrous phase equilibria (to 3 kbar) of an
652 andesite and basaltic andesite from western Mexico: constraints on water content and
653 conditions of phenocryst growth. Contributions to Mineralogy and Petrology, 130,
654 304-319.
655 Muller, T., Dohmen, R., Becker, H.W., ter Heege, J.H., and Chakraborty, S. (2013). Fe-Mg
656 interdiffusion rates in clinopyroxene: experimental data and implications for Fe-Mg
657 exchange geothermometers. Contributions to Mineralogy and Petrology, 166, 1563-
658 1576.
659 Nandedkar, R.H. (2014). Evolution of hydrous mantle-derived calc-alkaline liquids by
660 fractional crystallization at 0.7 and 0.4 GPa – An experimental study. Ph.D. thesis,
661 ETH.
662 Naney, M.T. (1983). Phase-Equilibria of Rock-Forming Ferromagnesian Silicates in Granitic
663 Systems. American Journal of Science, 283, 993-1033.
664 Nekvasil, H., Dondolini, A., Horn, J., Filiberto, J., Long, H., and Lindsley, D.H. (2004). The
665 origin and evolution of silica-saturated alkalic suites: an experimental study. Journal
666 of Petrology, 45, 693-721.
667 Nicholls, I.A., and Harris, K.L. (1980). Experimental Rare-Earth Element Partition-
668 Coefficients for Garnet, Clinopyroxene and Amphibole Coexisting with Andesitic and
669 Basaltic Liquids. Geochimica et Cosmochimica Acta, 44, 287-308.
670 Patino-Douce, A.E., and Beard, J.S. (1995). Dehydration-Melting of Biotite Gneiss and
671 Quartz Amphibolite from 3 to 15 Kbar. Journal of Petrology, 36, 707-738.

672 Pichavant, M., Di Carlo, I., Le Gac, Y., Rotolo, S.G., and Scaillet, B. (2009). Experimental
673 Constraints on the Deep Magma Feeding System at Stromboli Volcano, Italy. Journal
674 of Petrology, 50, 601-624.
675 Pichavant, M., Martel, C., Bourdier, J.L., and Scaillet, B. (2002). Physical conditions,
676 structure, and dynamics of a zoned magma chamber: Mount Pelee (Martinique, Lesser
677 Antilles Arc). Journal of Geophysical Research, 107(B5), 1-26.
678 Prouteau, G., and Scaillet, B. (2003). Experimental constraints on the origin of the 1991
679 Pinatubo dacite. Journal of Petrology, 44, 2203-2241.
680 Prouteau, G., Scaillet, B., Pichavant, M., and Maury, R.C. (1999). Fluid-present melting of
681 ocean crust in subduction zones. Geology, 27, 1111-1114.
682 Putirka, K.A. (2016). Amphibole thermometers and barometers for igneous systems, and
683 some implications for eruption mechanism of felsic magmas at arc volcanoes.
684 American Mineralogist, 101, 841-858.
685 Putirka, K.D. (2008). Thermometers and Barometers for Volcanic Systems. Reviews in
686 Mineralogy and Geochemistry, 69, 61-120.
687 Reubi, O., and Blundy, J. (2009). A dearth of intermediate melts at subduction zone
688 volcanoes and the petrogenesis of arc andesites. Nature, 461, 1269-1273.
689 Ridolfi, F., Puerini, M., Renzulli, A., Menna, M., and Toulkeridis, T. (2008). The magmatic
690 feeding system of El Reventador volcano (Sub-Andean zone, Ecuador) constrained by
691 texture, mineralogy and thermobarometry of the 2002 erupted products. Journal of
692 Volcanology and Geothermal Research, 176, 94-106.
693 Ridolfi, F., and Renzulli, A. (2012). Calcic amphiboles in calc-alkaline and alkaline magmas:
694 thermobarometric and chemometric empirical equations valid up to 1,130°C and
695 2.2 GPa. Contributions to Mineralogy and Petrology, 163, 877-895.

696 Ridolfi, F., Renzulli, A., and Puerini, M. (2010). Stability and chemical equilibrium of
697 amphibole in calc-alkaline magmas: an overview, new thermobarometric formulations
698 and application to subduction-related volcanoes. Contributions to Mineralogy and
699 Petrology, 160, 45-66.
700 Roeder, P.L., and Emslie, R.F. (1970). Olivine-Liquid Equilibrium. Contributions to
701 Mineralogy and Petrology, 29, 275-289.
702 Rutherford, M.J., and Devine, J.D. (2003). Magmatic conditions and magma ascent as
703 indicated by hornblende phase equilibria and reactions in the 1995-2002 Soufriere
704 Hills magma. Journal of Petrology, 44, 1433-1454.
705 Sato, H., Holtz, F., Behrens, H., Botcharnikov, R., and Nakada, S. (2005). Experimental
706 petrology of the 1991-1995 Unzen dacite, Japan. Part II: Cl/OH partitioning between
707 hornblende and melt and its implications for the origin of oscillatory zoning of
708 hornblende phenocrysts. Journal of Petrology, 46, 339-354.
709 Scaillet, B., and Evans, B.W. (1999). The 15 June 1991 eruption of Mount Pinatubo. I. Phase
710 equilibria and pre-eruption P-T-fO_2-fH_2O conditions of the dacite magma. Journal of
711 Petrology, 40, 381-411.
712 Schmidt, M.W. (1992). Amphibole Composition in Tonalite as a Function of Pressure: an
713 Experimental Calibration of the Al-in-Hornblende Barometer. Contributions to
714 Mineralogy and Petrology, 110, 304-310.
715 Shane, P., and Smith, V.C. (2013). Using amphibole crystals to reconstruct magma storage
716 temperatures and pressures for the post-caldera collapse volcanism at Okataina
717 volcano. Lithos, 156-159, 159-170.
718 Sisson, T.W. (1994). Hornblende-Melt Trace-Element Partitioning Measured by Ion
719 Microprobe. Chemical Geology, 117, 331-344.

720 Sisson, T.W., and Grove, T.L. (1993). Experimental Investigations of the Role of H2O in
721 Calc-Alkaline Differentiation and Subduction Zone Magmatism. Contributions to
722 Mineralogy and Petrology, 113, 143-166.
723 Skjerlie, K.P., and Johnston, A.D. (1996). Vapour-absent melting from 10 to 20 kbar of
724 crustal rocks that contain multiple hydrous phases: Implications for anatexis in the
725 deep to very deep continental crust and active continental margins. Journal of
726 Petrology, 37, 661-691.
727 Smith, D.J. (2014). Clinopyroxene precursors to amphibole sponge in arc crust. Nature
728 Communications, 5, 787.
729 Springer, W., and Seck, H.A. (1997). Partial fusion of basic granulites at 5 to 15 kbar:
730 Implications for the origin of TTG magmas. Contributions to Mineralogy and
731 Petrology, 127, 30-45.
732 Stamper, C.C., Blundy, J.D., Arculus, R.J., and Melekhova, E. (2014). Petrology of Plutonic
733 Xenoliths and Volcanic Rocks from Grenada, Lesser Antilles. Journal of Petrology,
734 55, 1353-1387.
735 Streck, M.J. (2008). Mineral Textures and Zoning as Evidence for Open System Processes.
736 Reviews in Mineralogy and Geochemistry, 69, 595-622.
737 Tiepolo, M., Vannucci, R., Bottazzi, P., Oberti, R., Zanetti, A., and Foley, S. (2000).
738 Partitioning of rare earth elements, Y, Th, U, and Pb between pargasite, kaersutite,
739 and basanite to trachyte melts: Implications for percolated and veined mantle.
740 Geochemistry Geophysics Geosystems, 1, 20431-20450.
741 Zhang, J., Davidson, J.P., Humphreys, M.C.S., Macpherson, C.G., and Neill, I. (2015).
742 Magmatic Enclaves and Andesitic Lavas from Mt. Lamington, Papua New Guinea:
743 Implications for Recycling of Earlier-fractionated Minerals through Magma Recharge.
744 Journal of Petrology, 56, 2223-2256.

FIGURE CAPTIONS

Fig. 1 (a-b) Experimental P-T run conditions, and (c-d) the relationship between temperature and melt SiO_2 content of the selected experiments. (a) and (c) illustrate the overlap in P-T-X conditions between the studies selected for calibrating chemometric equations and for testing the accuracy of the equations. (b) and (d) illustrate the corresponding amphibole species in terms of MgHst (magnesiohastingsite), MgHbl (magnesiohornblende), Parg (pargasite), Tsch (tschermakite) and Kaer (kaersutite), as well as amphiboles which are either non-calcic or have compositions out of equilibrium with the melt. The area outlined in (b) denotes the P-T window within which calcic amphiboles can crystallize and equilibrate with the melt. The arrow in (d) outlines the approximate liquid line of descent. (e-f) The relationships between amphibole crystal chemistry (Si_T, in apfu) and temperature and melt SiO_2 content (normalized to 100% anhydrous). See text for details.

Fig. 2 Calcic amphibole formula proportions of Parg, MgHst, Kaer, Tsch and MgHbl from the selected experimental studies. Symbols as for figure 1b, d.

Fig. 3 Test for equilibrium between amphibole and melt based on the Fe-Mg exchange coefficient (K_D). The amphibole and melt compositions are regarded as in equilibrium when K_D is within the range of 0.28 ± 0.11 (Putirka 2016). Symbols as for figure 1a, c.

Fig. 4 Major element compositions of melts from the selected experimental studies (normalized to 100% anhydrous). Symbols as for figure 1b, d.

Fig. 5 (a) Predicted melt MgO using Ridolfi and Renzulli (2012)'s model vs. measured MgO; (b) the overestimation of melt MgO at > 3 wt % is strongly dependent on the pressure (> 1,000 MPa) calculated with Ridolfi and Renzulli (2012)'s barometer model. Symbols as for figure 1b, d.

769 Fig. 6 Comparison between experimental and predicted melt compositions for the
770 calibration group (blue) and test group (red) using equations from Table 1, and results
771 calculated using Ridolfi and Renzulli (2012)'s chemometric equations (open circles). The
772 multiple regression analysis can reproduce the melt major element compositions with better
773 accuracy than Ridolfi and Renzulli (2012)'s model, which can generate a large offset from
774 measured melt compositions especially in the low-SiO_2 group and for TiO_2, FeO, MgO, CaO
775 and K_2O. Correlation coefficients and standard error of estimates are given in each plot for
776 the calibration results (R^2 and *SE*) and test results (r^2 and *se*). See text for details.

777 Fig. 7 Back-scattered electron SEM images of amphibole crystals from the Ongatiti
778 ignimbrite. (a) Type A crystal with non-distinct core and finely oscillatory zoned rim (no
779 compositional contrast). (b-c) Type B crystals with patchy zoned core (brighter patches of
780 MgHbl compositions and dark patches of MgHst compositions) and finely oscillatory zoned
781 rim (MgHbl), and with the presence of apatite and Fe-Ti oxides inclusions. The crystal in
782 panel (c) has a more distinct core-rim boundary than the crystal in panel (b).

783 Fig. 8 Melt compositions predicted from cores and rims of amphiboles in the Ongatiti
784 ignimbrite, and the measured compositions of coexisting matrix glasses of pumice clasts
785 (Cooper et al., 2014). The two vectors shown in each panel illustrate the effect of arbitrarily
786 changing the Mg# of two representative amphiboles (a MgHst with Mg# of 0.67, and a
787 MgHbl with Mg# of 0.57) as a result of Fe-Mg interdiffusion in modifying the predicted melt
788 compositions; small black symbols represent increments of 0.10 in Mg# as labelled in panel
789 *a* (see text for details). Panel (d) shows that the predicted MgO and SiO_2 in melts in
790 equilibrium with amphiboles in the Ongatiti ignimbrite fall into the field of compositional
791 array of global melt inclusions from Reubi and Blundy (2009).

792 Fig. 9 (a) Melt compositions inferred from amphibole in clinopyroxenite, hornblendite
793 and hornblende gabbro cumulate xenoliths from Grenada, as well as non-cumulate
794 hornblende gabbro (data from Stamper et al. 2014). Curves in (b) illustrate the results of
795 MELTS modelling with a range of pressure input (from Stamper et al. 2014). The variations
796 of the predicted melt CaO content and MgO content are consistent with low- to moderate-
797 pressure fractionation. As with melt prediction results of Ongatiti amphiboles, the predicted
798 MgO and SiO_2 in melts in equilibrium with amphiboles in Grenada cumulates and the non-
799 cumulate gabbro also plot within the compositional array of global melt inclusions (Reubi
800 and Blundy 2009). Panel (f) also illustrates that the predicted melt MgO and SiO_2
801 compositions project back towards initial melts parental to clinopyroxenite/hornblendite
802 (open square) and hornblende gabbro (open circle), inferred from earlier experimental studies
803 (Stamper et al. 2014). The melt compositions predicted using Ridolfi and Renzulli (2012)'s
804 model are plotted as areas outlined in dotted lines. See further discussion in the text.

805

806

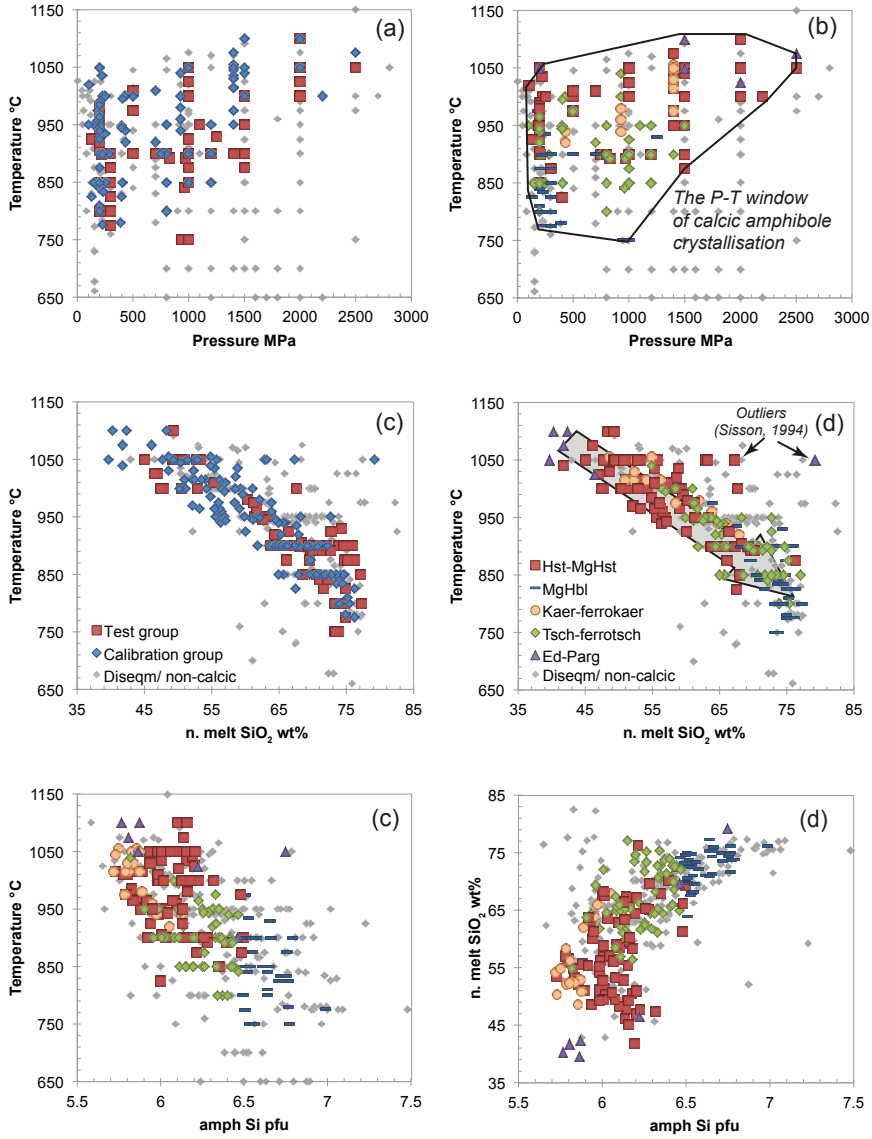
(a)
(b)
(c)
(d)
Temperature °C
Pressure MPa
The P-T window
of calcic amphibole
crystallisation
Outliers
(Sisson, 1994)
Test group
Calibration group
Diseqm/ non-calcic
Hst-MgHst
MgHbl
Kaer-ferrokaer
Tsch-ferrotsch
Ed-Parg
n. melt SiO2 wt%
amph Si pfu

Figure 1

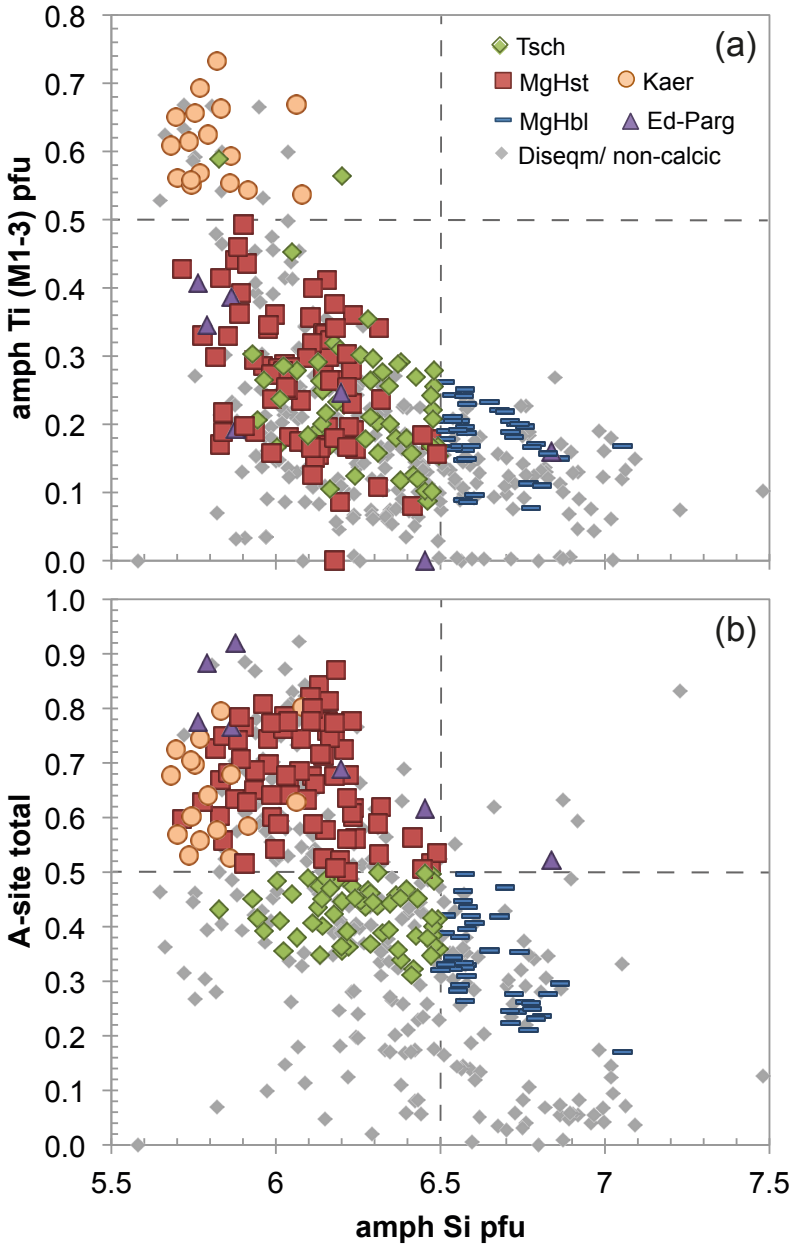
(a)
Tsch
MgHst
Kaer
MgHbl
Ed-Parg
Diseqm/ non-calcic
amph Ti (M1-3) pfu
0.0
0.1
0.2
0.3
0.4
0.5
0.6
0.7
0.8
(b)
A-site total
0.0
0.1
0.2
0.3
0.4
0.5
0.6
0.7
0.8
0.9
1.0
5.5
6
6.5
7
7.5
amph Si pfu

Figure 2

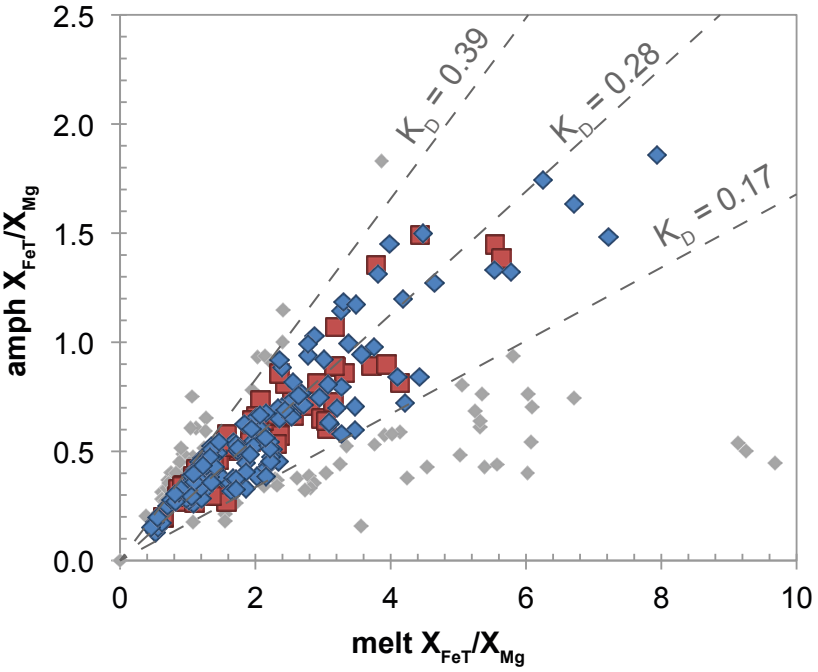
2.5
2.0
1.5
1.0
0.5
0.0
0
2
4
6
8
10
amph X_{FeT}/X_{Mg}
melt X_{FeT}/X_{Mg}
$K_D = 0.39$
$K_D = 0.28$
$K_D = 0.17$

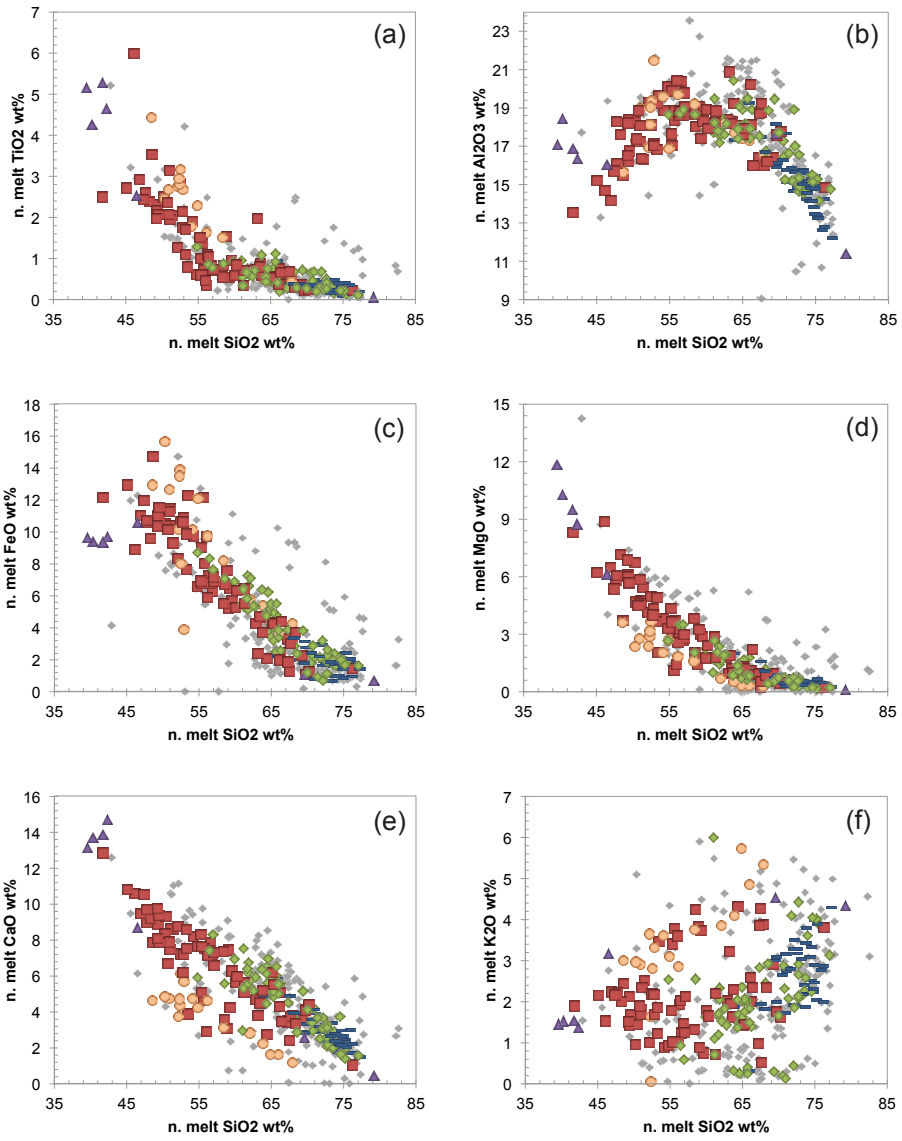
(a)
n. melt TiO2 wt%
n. melt SiO2 wt%
(b)
n. melt Al2O3 wt%
n. melt SiO2 wt%
(c)
n. melt FeO wt%
n. melt SiO2 wt%
(d)
n. melt MgO wt%
n. melt SiO2 wt%
(e)
n. melt CaO wt%
n. melt SiO2 wt%
(f)
n. melt K2O wt%
n. melt SiO2 wt%

Figure 4

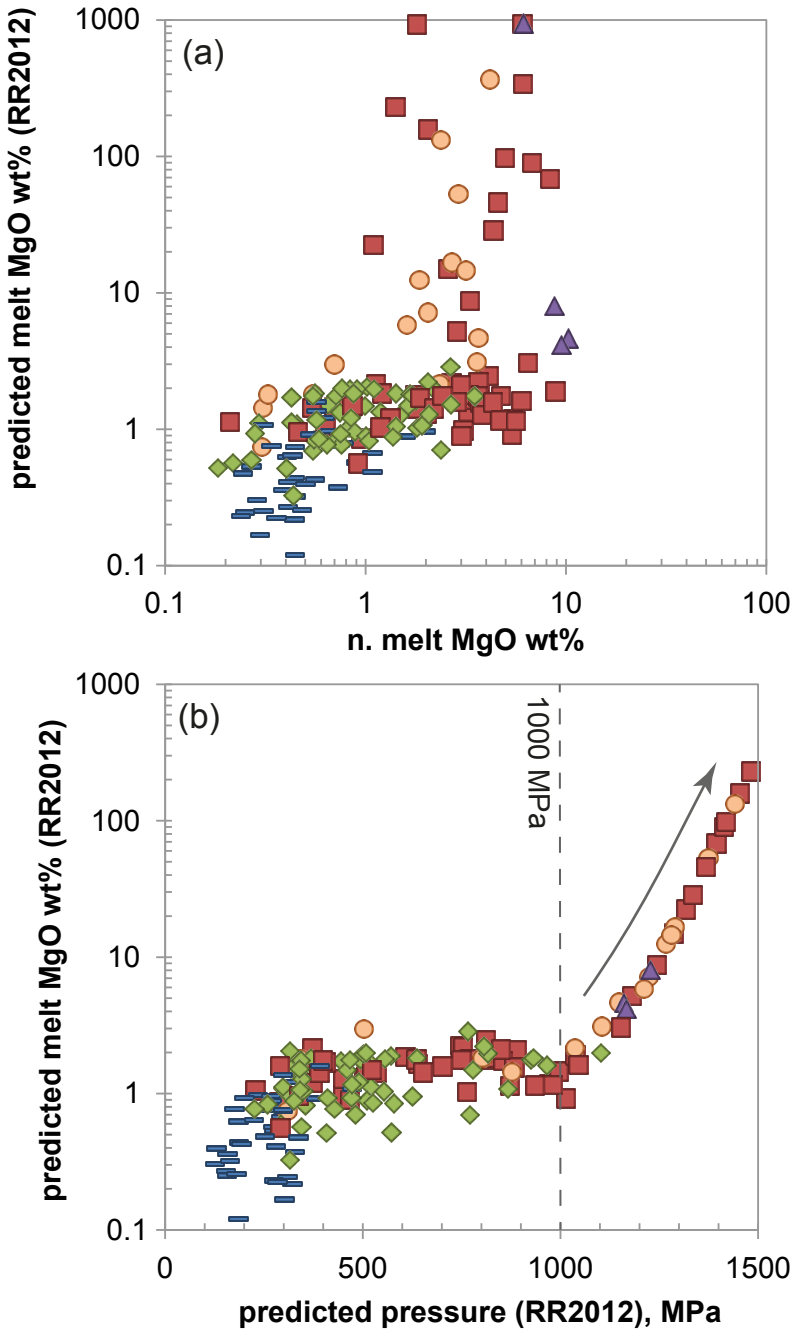
(a)
predicted melt MgO wt% (RR2012)
n. melt MgO wt%
1000
100
10
1
0.1
0.1
1
10
100
(b)
1000 MPa
predicted melt MgO wt% (RR2012)
predicted pressure (RR2012), MPa
0
500
1000
1500

Figure 5

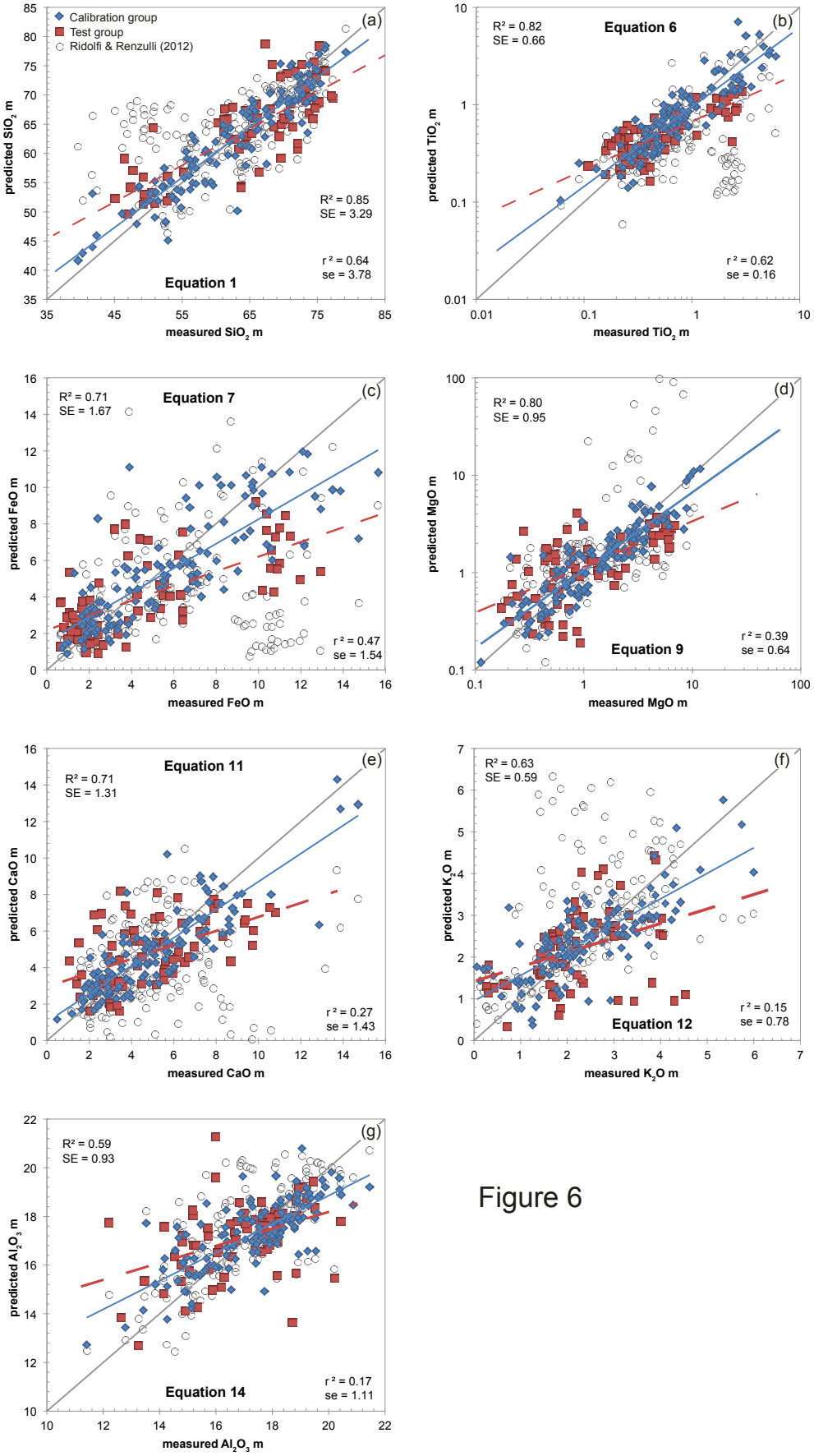
(a)
Calibration group
Test group
Ridolfi & Renzulli (2012)
R² = 0.85
SE = 3.29
r ² = 0.64
se = 3.78
Equation 1
predicted SiO2 m
measured SiO2 m
(b)
R² = 0.82
SE = 0.66
Equation 6
r ² = 0.62
se = 0.16
predicted TiO2 m
measured TiO2 m
(c)
R² = 0.71
SE = 1.67
Equation 7
r ² = 0.47
se = 1.54
predicted FeO m
measured FeO m
(d)
R² = 0.80
SE = 0.95
Equation 9
r ² = 0.39
se = 0.64
predicted MgO m
measured MgO m
(e)
R² = 0.71
SE = 1.31
Equation 11
r ² = 0.27
se = 1.43
predicted CaO m
measured CaO m
(f)
R² = 0.63
SE = 0.59
Equation 12
r ² = 0.15
se = 0.78
predicted K2O m
measured K2O m
(g)
R² = 0.59
SE = 0.93
Equation 14
r ² = 0.17
se = 1.11
predicted Al2O3 m
measured Al2O3 m

Figure 6

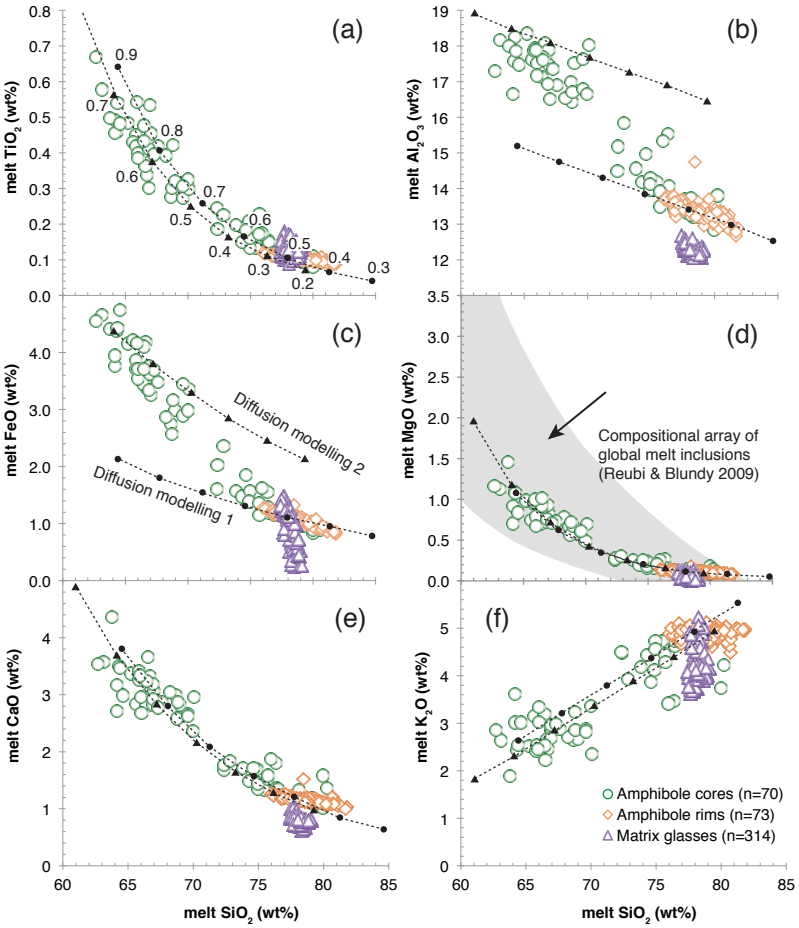
(a)
(b)
(c)
(d)
(e)
(f)
melt TiO2 (wt%)
melt Al2O3 (wt%)
melt FeO (wt%)
melt MgO (wt%)
melt CaO (wt%)
melt K2O (wt%)
melt SiO2 (wt%)
melt SiO2 (wt%)
0.9
0.7
0.8
0.6
0.7
0.5
0.6
0.4
0.5
0.3
0.4
0.2
0.3
Diffusion modelling 2
Diffusion modelling 1
Compositional array of
global melt inclusions
(Reubi & Blundy 2009)
Amphibole cores (n=70)
Amphibole rims (n=73)
Matrix glasses (n=314)

Figure 8 new

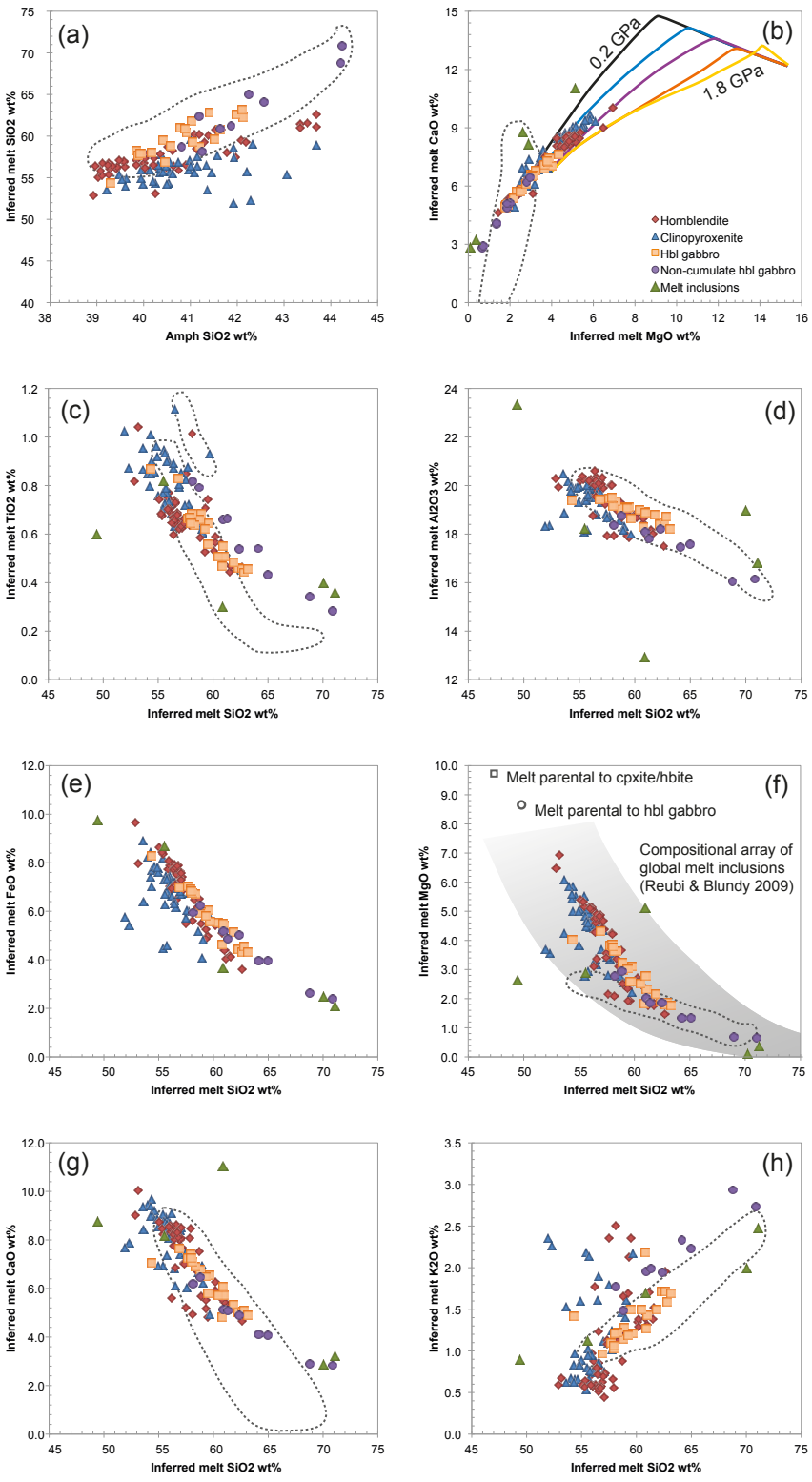
(a)
Inferred melt SiO2 wt%
Amph SiO2 wt%
(b)
0.2 GPa
1.8 GPa
Inferred melt CaO wt%
Inferred melt MgO wt%
Hornblendite
Clinopyroxenite
Hbl gabbro
Non-cumulate hbl gabbro
Melt inclusions
(c)
Inferred melt TiO2 wt%
Inferred melt SiO2 wt%
(d)
Inferred melt Al2O3 wt%
Inferred melt SiO2 wt%
(e)
Inferred melt FeO wt%
Inferred melt SiO2 wt%
(f)
Melt parental to cpxite/hbite
Melt parental to hbl gabbro
Compositional array of global melt inclusions (Reubi & Blundy 2009)
Inferred melt MgO wt%
Inferred melt SiO2 wt%
(g)
Inferred melt CaO wt%
Inferred melt SiO2 wt%
(h)
Inferred melt K2O wt%
Inferred melt SiO2 wt%

Figure 9

Table 1 Materials, conditions and run products of the selected experimental studies

References for calibration	Rock type	*N* (130)	*P* MPa	*T* ºC	Amphibole Species	RR2012	E2014
Adam & Green 1994	basanite	5	500-2,000	1,000-1,100	MgHst	Y	
Alonso-Perez et al., 2009	andesite	12	800-1,200	800-950	Tsch		
Barclay & Carmichael 2004	trachybasalt	3	104-223	1000-1035	MgHst		Y
Bogaerts et al. 2006	granodiorite	2	404	850	Tsch		Y
Costa et al. 2004	dacite	4	200-206	850-900	MgHbl, MgHst	Y	Y
Dalpé & Baker, 2000	basanite-basalt	7	1,500-2,500	1,000-1,100	MgHst, Parg	Y	
Gardner et al., 1995	dacite	6	150-250	850	Tsch, MgHbl	Y	
Green & Pearson 1985	andesite	4	750-2,000	900-1,050	MgHst, Parg, Tsch		
Grove et al. 2003	Mg andesite	1	200	990	MgHst		
Hilyard et al. 2000	dacite-tonalite	5	200-500	900-945	MgHst, MgHbl, Parg, Tsch		
Klein et al. 1997	dacite	2	1,000	850-900	Tsch		
Martel et al. 2013	trachyte	2	200-400	825-900	MgHst		Y
Moore & Carmichael, 1998	basaltic andesite-andesite	6	101-250	900-1,000	MgHbl, Tsch	Y	
Nandedkar 2014	basaltic andesite-rhyolite	3	700	920-1,010	Tsch, MgHst		
Nekvasil et al., 2004	basalt-dacite	8	430-930	920-1040	Kaer, Tsch	Y	
Nicholls & Harris 1980	basalt-andesite	1	1,000	900	Tsch		
Pichavant et al. 2002	basaltic andesite	6	399-427	945-1,000	Tsch	Y	Y
Pichavant et al. 2009	quartz diorite	3	200	850	MgHst, Tsch		
Rutherford & Devine 2003	andesite	3	200	810-840	MgHbl	Y	Y
Sato et al. 2005	dacite	5	200	850	MgHbl, Tsch	Y	Y
Scaillet & Evans 1999	dacite	7	224-389	776-899	MgHbl, Tsch	Y	Y
Sisson 1994	basalt-andesite-dacite	4	200	1050	MgHbl, MgHst		
Sisson & Grove 1993	high-Al basalt	11	200	925-970	MgHst		Y
Tiepolo et al. 2000	basalt-andesite	20	1400	950-1075	Kaer, MgHst, Parg		

Overall dataset contains 43 Hst-MgHst, 39 Tsch, 17 Kaer-Ferrokaersutite, 24 MgHbl-ferrohornblende, and 5 Edenite-Prg (n = 128).
Melt compositional range 39.6 - 79.9 wt% SiO2 and 0.1 - 11.9 wt% MgO.

References for test	Rock type	*N* (74)	*P* MPa	*T* ºC	Amphibole Species	RR2012	E2014
Adam & Green 2006	basanite	1	1,000	1,025	MgHst		
Adam et al. 1993	basanite-basalt	4	1,000-2,000	1,000-1,050	MgHst, Parg		
Blatter & Carmichael, 2001	andesite	2	132-194	925-950	Tsch		
Carroll & Wyllie, 1989	tonalite	2	1,500	900-950	MgHst, Parg		
Ernst & Liu, 1998	basalt	5	800-1,400	900-950	Tsch		
Fujinawa & Green, 1997	basalt-andesite	16	500-2,000	900-1,100	MgHst, Parg, Tsch		
Grove et al., 1997	basalt	5	200	905-980	Tsch		
Holtz et al., 2005	dacite	10	200-300	775-875	MgHst, Tsch, MgHbl		
Kawamoto, 1996	basaltic andesite	2	500	975	Parg, Tsch		
Naney, 1983	granodiorite	2	800	900	MgHst, Parg		
Patino-Douce & Beard, 1995	quartz amphibolite	6	300-1,250	875-930	MgHbl, Tsch		
Prouteau & Scaillet, 2003	dacite	9	830-970	750-892	MgHst, Tsch, MgHbl		
Prouteau et al., 1999	dacite	2	220-1,000	750-899	MgHbl		
Skjerlie & Johnston, 1996	andesitic metavolcanoclastics	4	1,000-1,500	850-900	MgHst, Tsch		
Springer & Seck, 1997	granulite	2	1,000-1,500	900-1,000	Tsch, Parg		

Overall dataset contains 30 MgHst, 21 Tsch, 2 Prg, 18 MgHbl and 1 Ferrohornblende (n = 72). Melt compositional range 45.1 - 77.3 wt% SiO2 and 0.2 - 6.9 wt% MgO.

Y indicates the data of the reference are also used in the calibrations of chemometric equations in Ridolfi & Renzulli (2012)'s and Erdmann et al. (2014)'s study.

Table 2 Results of multiple linear regressions used for estimating melt major element compositions on the basis of temperature and calcic-amphibole component. N = 130

Eq.	Dependent variable	Parameters used	Range of variation	Constant	Independent variable coefficients											*Multiple R^2*	*SE (wt %)*	*se (wt%)*
					T ºC	Si	lnSi	Al (vi)	Mg	Fe3+	Fe2+	Fetot	Ti	Ca	Na (A)			
1	SiO_2 (wt %)	$lnSi_T$	39.6 - 79.2	-736.7170			288.7330	56.5360	27.1690	62.6650	34.8140		83.9890	44.2250	14.0490	0.849	3.29	3.78
2	SiO_2 (wt %)	$lnSi_T$	39.6 - 79.2	-399.9891			212.9463	11.7464		23.5653	6.8467		24.7743	24.4399		0.834	3.38	4.19
3	SiO_2 (wt %)	$lnSi_T$, Fe_T	39.6 - 79.2	-228.0000	**0.0107**		165.0000		-7.2190							0.791	3.70	4.37
4	SiO_2 (wt %)	$lnSi_T$, Fe_T	39.6 - 79.2	-222.6140			167.5170		-7.1560							0.782	3.75	4.51
5	$lnTiO_2$	Si_T	-2.8 - 1.8	23.4870	**-0.0011**	-2.5692		-1.3919		-2.1195	-1.0511			-2.0634	-1.5961	0.820	0.62	0.17
6	$lnTiO_2$	Si_T	-2.8 - 1.8	22.4650		-2.5975		-1.1550		-2.2329	-1.0319			-1.9825	-1.5591	0.813	0.66	0.16
7	ln FeO	Si_T	-0.34 - 2.75	24.4613		-2.7231		-1.0735		-1.0466	-0.2580		-1.9360	-2.5228		0.712	1.67	1.54
8	lnFeO	Si_T, Fe_T	-0.34 - 2.75	15.6864		-2.0966			0.3646					-1.3313		0.699	1.76	1.35
9	lnMgO	Si_T	-2.19 - 2.47	12.6618		-2.6319		1.0500	1.2604							0.798	0.96	0.64
10	CaO (wt %)	Si_T	0.5 - 14.7	41.2784		-7.1955			3.6412						-5.0437	0.606	1.35	1.23
11	lnCaO	Si_T	-0.7 - 2.7	6.4192		-1.1737		1.3198	0.6773							0.711	1.31	1.43
12	K_2O (wt %)	Si_T	<6.0	100.5909		-4.3246		-17.8256	-10.0901	-15.6830	-8.8004		-19.7448	-6.3727	-5.8069	0.630	0.59	0.78
13	K_2O (wt %)	Si_T, Fe_T	<6.0	-16.5300		1.6878						1.2354	5.0404	2.9703		0.434	0.57	0.69
14	Al_2O_3 (wt %)	Si_T	11.4 - 21.5	4.5730				6.9408	1.0059	4.5448			5.9679		7.1501	0.585	0.93	1.11

Normal font indicates p-value < 0.01; bold font indicates the *p-value* of the parameter or the constant is 0.01 ≤ *p-value* < 0.05

Table 3 Equilibrium test for pairs of amphibole rims and matrix glasses from pumice clasts in Ongatiti ignimbrite

Pumice #		Am. wt %	Am.sd.	Gl. wt %	Gl.sd.	Pred. wt %	Pred.sd.	MR.se.	Diff.	Diff%	Diff.>MR.se?
GC1	SiO_2	44.62	0.33	77.75	0.16	77.37	0.82	3.59	-0.38	-0.5%	
(N.amph = 28)	TiO_2	1.77	0.04	0.13	0.02	0.11	0.01	0.66	-0.02	-14.5%	
(N.gl = 22)	Al_2O_3	7.68	0.16	12.34	0.11	13.61	0.11	1.13	1.27	10.3%	Y
	FeO	19.40	0.30	1.30	0.07	1.16	0.07	1.76	-0.14	-10.5%	
	MgO	10.17	0.19	0.11	0.01	0.13	0.01	0.95	0.02	21.9%	
	CaO	10.59	0.08	0.85	0.02	1.21	0.03	1.38	0.36	**41.8%**	
	K_2O	0.65	0.03	4.08	0.12	4.91	0.09	0.60	0.83	20.2%	Y
	Na_2O	1.98	0.05	3.41	0.17						
	MnO	0.48	0.03	0.04	0.02						
P2023	SiO_2	45.93	0.39	77.86	0.24	80.37	0.63	3.59	2.51	3.2%	
(N.amph = 15)	TiO_2	1.75	0.06	0.14	0.02	0.10	0.01	0.66	-0.04	-28.6%	
(N.gl = 28)	Al_2O_3	7.31	0.17	12.39	0.08	13.19	0.14	1.13	0.80	6.5%	
	FeO	19.33	0.64	1.20	0.19	0.95	0.04	1.76	-0.25	-20.8%	
	MgO	10.37	0.37	0.10	0.02	0.10	0.01	0.95	0.00	-1.4%	
	CaO	10.74	0.07	0.92	0.07	1.11	0.05	1.38	0.19	20.8%	
	K_2O	0.61	0.04	3.86	0.15	4.91	0.15	0.60	1.05	**27.3%**	Y
	Na_2O	1.81	0.06	3.50	0.11						
	MnO	0.41	0.02	0.03	0.02						
P2026	SiO_2	45.07	0.44	78.23	0.23	77.57	2.40	3.59	-0.66	-0.8%	
(N.amph = 5)	TiO_2	1.82	0.08	0.13	0.02	0.11	<0.01	0.66	-0.02	-16.2%	
(N.gl = 28)	Al_2O_3	7.48	0.18	12.30	0.07	13.27	0.08	1.13	0.97	7.8%	
	FeO	20.11	0.29	0.73	0.27	1.12	0.07	1.76	0.39	**53.6%**	
	MgO	10.45	0.22	0.05	0.03	0.13	0.01	0.95	0.08	**160.4%**	Y
	CaO	10.79	0.04	0.74	0.06	1.18	0.03	1.38	0.44	**59.8%**	Y
	K_2O	0.63	0.04	4.65	0.33	4.82	0.12	0.60	0.17	3.7%	
	Na_2O	1.92	0.06	3.15	0.20						
	MnO	0.44	0.02	0.01	0.01						
P2027	SiO_2	45.15	0.46	77.97	0.43	79.85	1.12	3.59	1.88	2.4%	
(N.amph = 33)	TiO_2	1.82	0.06	0.13	0.01	0.10	0.01	0.66	-0.03	23.0%	
(N.gl = 9)	Al_2O_3	7.23	0.22	12.50	0.14	13.10	0.19	1.13	0.60	4.8%	
	FeO	19.53	0.31	0.72	0.40	0.99	0.90	1.76	0.27	**37.6%**	
	MgO	10.24	0.25	0.04	0.03	0.11	0.01	0.95	0.07	**160.6%**	Y
	CaO	10.66	0.11	0.77	0.07	1.11	0.05	1.38	0.34	**43.2%**	Y
	K_2O	0.60	0.04	4.79	0.34	4.87	0.10	0.60	0.08	1.7%	
	Na_2O	1.78	0.09	3.06	0.19						
	MnO	0.37	0.02	0.01	0.01						
P2184	SiO_2	44.74	0.35	78.63	0.30	79.01	0.79	3.59	0.38	0.5%	
(N.amph = 30)	TiO_2	1.81	0.11	0.13	0.01	0.10	0.01	0.66	-0.03	24.0%	
(N.gl = 29)	Al_2O_3	7.60	0.26	12.21	0.08	13.34	0.28	1.13	1.13	9.3%	
	FeO	19.97	0.54	0.74	0.30	1.10	0.08	1.76	0.36	**48.4%**	
	MgO	9.95	0.31	0.06	0.03	0.12	0.02	0.95	0.06	**95.6%**	Y
	CaO	10.64	0.11	0.79	0.02	1.15	0.08	1.38	0.36	**44.9%**	Y
	K_2O	0.64	0.04	4.09	0.13	4.84	0.20	0.60	0.75	18.3%	
	Na_2O	1.83	0.06	3.32	0.13						
	MnO	0.38	0.02	0.02	0.01						

Compositions of amphibole rims and matrix glasses, as well as predicted melt in equilibrium with amphibole rims, are given as average values of multiple analyses from each pumice clast, with standard deviation; Diff. indicates the disparity between the predicted melt compositions and matrix glasses; Diff% = Diff./Gl. wt %; Diff% is highlighted in bold font when it is > 20.0%; Y indicates Diff. is larger than the se of the chemometric equation which is used for predicting melt compositions.

Table 4 Results of Fe-Mg interdiffusion modelling carried out on amphiboles from pumice clasts of the Ongatiti ignimbrite

	Amphibole compositions	Originally predicted melt compositions	Melt compositions predicted using different Mg#					
			0.80	0.70	0.60	0.50	0.40	0.30
SiO_2	41.83	65.21	61.03	64.09	67.14	70.20	73.26	76.32
TiO_2	3.33	0.48	0.85	0.56	0.37	0.25	0.16	0.11
Al_2O_3	11.62	18.35	18.90	18.50	18.10	17.69	17.29	16.89
FeO_t	13.32	4.16	5.08	4.39	3.80	3.28	2.84	2.45
MgO	12.10	0.99	1.97	1.19	0.72	0.43	0.26	0.16
CaO	11.09	3.37	4.88	3.72	2.84	2.17	1.65	1.26
K_2O	0.43	2.53	1.82	2.34	2.85	3.37	3.89	4.40
SiO_2	44.65	77.42	67.77	71.16	74.55	77.93	81.32	84.71
TiO_2	1.82	0.11	0.41	0.26	0.16	0.10	0.07	0.04
Al_2O_3	7.66	13.49	14.75	14.30	13.86	13.41	12.97	12.52
FeO_t	19.70	1.14	1.80	1.53	1.30	1.11	0.94	0.80
MgO	10.00	0.13	0.62	0.35	0.20	0.12	0.07	0.04
CaO	10.64	1.20	2.83	2.09	1.55	1.15	0.85	0.63
K_2O	0.65	4.85	3.23	3.81	4.38	4.95	5.52	6.09

The first amphibole is a MgHst with 0.76 Mg#, 0.33 wt% MnO and 2.89 wt % Na_2O; the second amphibole is MgHbl with 0.53 Mg#, 0.42 wt% MnO and 1.98 wt % Na_2O.